




Dome structure in pressure dependence of superconducting transition temperature for $\text{HgBa}_2\text{Ca}_2\text{Cu}_3\text{O}_8$: Studies by *ab initio* low-energy effective Hamiltonian


Jean-Baptiste Morée ^{1,2}, Youhei Yamaji ³, and Masatoshi Imada ^{1,4}

¹Research Institute for Science and Engineering, Waseda University, 3-4-1, Okubo, Shinjuku, Tokyo 169-8555, Japan

²RIKEN Center for Emergent Matter Science, 2-1 Hirosawa, Wako, Saitama 351-0198, Japan

³Research Center for Materials Nanoarchitectonics (MANA) and Center for Green Research on Energy and Environmental Materials (GREEN), National Institute for Materials Science (NIMS), Namiki, Tsukuba-shi, Ibaraki 305-0044, Japan

⁴Physics Division, Sophia University, Kioi-cho, Chiyoda-ku, Tokyo 102-8554, Japan

 (Received 26 December 2023; revised 12 April 2024; accepted 23 April 2024; published 13 May 2024)

The superconducting (SC) cuprate $\text{HgBa}_2\text{Ca}_2\text{Cu}_3\text{O}_8$ (Hg1223) has the highest SC transition temperature T_c among cuprates at ambient pressure P_{amb} , namely, $T_c^{\text{opt}} \simeq 138$ K experimentally at the optimal hole doping concentration. T_c^{opt} further increases under pressure P and reaches 164 K at optimal pressure $P_{\text{opt}} \simeq 30$ GPa, then T_c^{opt} decreases with increasing $P > P_{\text{opt}}$ generating a dome structure [Gao *et al.*, *Phys. Rev. B* **50**, 4260(R) (1994)]. This nontrivial and nonmonotonic P dependence of T_c^{opt} calls for a theoretical understanding and mechanism. To answer this open question, we consider the *ab initio* low-energy effective Hamiltonian (LEH) for the antibonding (AB) $\text{Cu}3d_{x^2-y^2}/\text{O}2p_\sigma$ band derived generally for the cuprates. In the AB LEH for cuprates with $N_\ell \leq 2$ laminated CuO_2 planes between block layers, it was proposed that T_c^{opt} is determined by a universal scaling $T_c^{\text{opt}} \simeq 0.16|t_1|F_{\text{SC}}$ [Schmid *et al.*, *Phys. Rev. X* **13**, 041036 (2023)], where t_1 is the nearest-neighbor hopping, and the SC order parameter at optimal hole doping F_{SC} mainly depends on the ratio $u = U/|t_1|$ where U is the onsite effective Coulomb repulsion: The u dependence of F_{SC} has a peak at $u_{\text{opt}} \simeq 8.5$ and a steep decrease with decreasing u in the region $u < u_{\text{opt}}$ irrespective of materials dependent on other *ab initio* parameters. In this paper, we show that $|t_1|$ increases with P , whereas u decreases with P in the *ab initio* Hamiltonian of Hg1223. Based on these facts, we show that the domelike P dependence of T_c^{opt} can emerge at least qualitatively if we assume Hg1223 with $N_\ell = 3$ follows the same universal scaling for T_c^{opt} , and Hg1223 is located at the slightly strong coupling region $u \gtrsim u_{\text{opt}}$ at P_{amb} and $u \simeq u_{\text{opt}}$ at P_{opt} by taking account of expected corrections to our *ab initio* calculation. The consequence of these assumptions is the following: With increasing P within the range $P < P_{\text{opt}}$, the increase in T_c^{opt} is accounted for by the increase in $|t_1|$, whereas F_{SC} is insensitive to the decrease in u around $\simeq u_{\text{opt}}$ and hence to P as well. At $P > P_{\text{opt}}$, the decrease in T_c^{opt} is accounted for by the decrease in u below u_{opt} , which causes a rapid decrease in F_{SC} dominating over the increase in $|t_1|$. We further argue the appropriateness of these assumptions based on the insight from studies on other cuprate compounds in the literature. In addition, we discuss the dependencies of u and $|t_1|$ on each crystal parameter (CP), which provides hints for design of even higher T_c^{opt} materials.

DOI: [10.1103/PhysRevResearch.6.023163](https://doi.org/10.1103/PhysRevResearch.6.023163)

I. INTRODUCTION

Unconventional SC occurs in cuprates [1] with a diverse distribution of T_c^{opt} . At P_{amb} , known values of T_c^{opt} range from $T_c^{\text{opt}} \simeq 6$ K in $\text{Bi}_2\text{Sr}_2\text{CuO}_6$ (Bi2201) [2] to $T_c^{\text{opt}} \simeq 138$ K in $\text{HgBa}_2\text{Ca}_2\text{Cu}_3\text{O}_8$ (Hg1223) [3,4]. T_c^{opt} further increases under pressure. In the case of Hg1223 and other Hg-based cuprates, T_c^{opt} has a domelike structure as a function of P [3,5]. An example is shown in Fig. 1(b) for Hg1223: T_c^{opt} increases with pressure and shows the maximum 164 K at $P_{\text{opt}} \simeq 30$ GPa [3,6], which is the highest known value of T_c^{opt} in the cuprates.

A wide range of $T_c^{\text{opt}} \simeq 6$ –164 K in the cuprates has inspired studies on chemical substitution and pressure

application to gain insights into the microscopic mechanism of the diversity in T_c^{opt} . For example, for Y-based [8–16] and Hg-based [17,18] high- T_c cuprates, the uniaxial pressures P_a and P_c were applied. (In this paper, P_a refers to the simultaneous compression along axes **a** and **b** in Fig. 2, while keeping $|\mathbf{a}| = |\mathbf{b}|$, and P_c refers to the compression along axis **c**. The axes are represented in Fig. 2 for the tetragonal cell in Hg1223.) This decomposition of pressure revealed, in the case of $\text{HgBa}_2\text{CuO}_4$ (Hg1201, $T_c^{\text{opt}} \simeq 94$ K [19]), that T_c^{opt} decreases with out-of- CuO_2 plane contraction caused by P_c ($\partial T_c^{\text{opt}}/\partial P_c \simeq -3$ K/GPa) but increases with in-plane contraction caused by P_a ($\partial T_c^{\text{opt}}/\partial P_a \simeq 5$ K/GPa) [17].

However, microscopic mechanisms leading to the P dependence of T_c^{opt} are not well understood, while understanding the mechanism of them certainly helps future materials design. Since it is difficult to isolate these hidden mechanisms by experiments only, further theoretical studies of cuprates under P are desirable.

Published by the American Physical Society under the terms of the [Creative Commons Attribution 4.0 International license](https://creativecommons.org/licenses/by/4.0/). Further distribution of this work must maintain attribution to the author(s) and the published article's title, journal citation, and DOI.

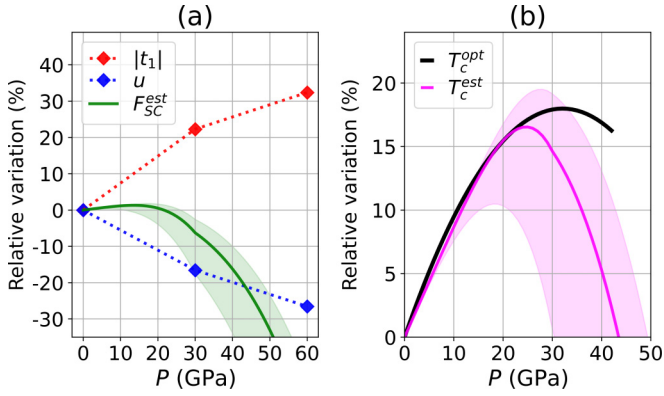


FIG. 1. Summary of the main results and theoretical prediction of the dome structure in the P dependence of T_c . (a) P dependence of $|t_1|$ and u deduced at the most sophisticated cGW-SIC+LRFB level. These values are estimated from the calculated results at the cGW-SIC level by supplementing the correction from the cGW-SIC to the cGW-SIC+LRFB levels defined in Eqs. (2) and (3). The pressure P is measured from P_{amb} . P dependence of F_{SC} estimated at the cGW-SIC+LRFB level denoted as F_{SC}^{est} is also plotted, where F_{SC}^{est} is deduced from the universal u dependence found in Ref. [7] and using u for Hg1223 shown here. See below Eqs. (2) and (3) for the detailed corrections of cGW-SIC and cGW-SIC+LRFB levels, where the notations for the quantities improved in such ways are denoted as $u_{cGW-SIC+LRFB}$ ($u_{cGW-SIC}$) and $|t_1|_{cGW-SIC+LRFB}$ ($|t_1|_{cGW-SIC}$) instead of u and $|t_1|$, respectively, to indicate the cGW-SIC+LRFB (cGW-SIC) levels explicitly. Diamond symbols show results at $P = P_{amb}$, 30 GPa and 60 GPa, and dashed lines show linear interpolations between diamonds. (b) Experimental T_c^{opt} [3] (black curve) and the present theoretical optimum T_c denoted as T_c^{est} deduced from Eq. (1) proposed in Ref. [7] by replacing F_{SC} with F_{SC}^{est} . Shaded areas in (a) and (b) indicate the uncertainty described below Eqs. (2) and (3). Qualitative dome structure of T_c^{opt} is reproduced in the present prediction, T_c^{est} .

In this paper, we propose a microscopic mechanism for the P dependence of T_c^{opt} for the carrier-doped Hg1223 based on an *ab initio* study. For *ab initio* studies, the density functional theory (DFT) has been widely applied [20,21]. However, its insufficiency in strongly correlated electron systems is also well known. Instead, we apply the multiscale *ab initio* scheme for correlated electrons (MACE) [22–28], which has succeeded in correctly reproducing the SC properties of the cuprates [7,28–30] at ambient pressure and has motivated further studies on hypothetical Ag-based compounds [31].

MACE consists of a three-step procedure that determines the LEH parameters for the single-band AB Hamiltonian; this procedure has several different accuracy levels, which are defined below and whose details are given in Appendix A. At the earliest stage of the MACE, the simplest level denoted as LDA+cRPA [22,23] or GGA+cRPA was employed; at this level, we start from the electronic structure at the local density approximation (LDA) or generalized gradient approximation (GGA) level, and the effective interaction parameters are calculated on the level of the constrained random phase approximation (cRPA) [22]. The next level is denoted as cGW-SIC [27], in which the starting electronic structure is preprocessed from the LDA or GGA level to the one-shot GW

level, and the one-particle part is improved using the constrained GW (cGW) [25] and the self-interaction correction (SIC) [26]. The most recent and accurate level is denoted as cGW-SIC+LRFB [28], which is essentially the same as the cGW-SIC, except that the GW electronic structure is further improved: The level renormalization feedback (LRFB) [28] is used to correct the onsite $Cu3d_{x^2-y^2}$ and $O2p_\sigma$ energy levels.

Although the cGW-SIC+LRFB level is the most accurate and was used to reproduce the SC properties of the cuprates [7,28–30], we mainly employ the simplest GGA+cRPA version for the purpose of the present paper, because the qualitative trend of the parameters can be captured by this simplest framework. (See Appendix A for a more detailed discussion.) We also reinforce the analysis by deducing more refined cGW-SIC+LRFB level in a limited case from the explicit cGW-SIC level calculations to remove the known drawback of GGA+cRPA as we detail later.

We derive and analyze the pressure dependence of AB LEH parameters including various intersite hoppings and interactions; however, we restrict the main discussion to $|t_1|$ and u , since they are the principal parameters that control T_c in the proposal [7]. Other LEH parameters are given in the Supplemental Material [32]. In the following, we mainly discuss $|t_1^{avg}|$ and u^{avg} , which are the *ab initio* values of $|t_1|$ and u at GGA+cRPA level, averaged over the inner and outer CuO_2 planes. (See Fig. 2 for a representation of the CuO_2 planes.)

This paper is organized as follows. In Sec. II, the central results of the present paper are outlined to capture the essence of the results before detailed presentation. In Sec. III, we give the crystal structure of Hg1223, the hole concentration, and a reminder of the GGA+cRPA scheme. In Sec. IV, we give the DFT electronic structure at the GGA level as a function of P . In Sec. V, we show the pressure dependence of AB LEH parameters at the GGA+cRPA level. In Sec. VI, we discuss the adequacy of the assumptions made in Sec. II. We also discuss the consistency of our results with the experimental P dependence of T_c^{opt} in Fig. 1. Our summary and conclusion are given in Sec. VII. In Appendix A, methodological details of the MACE scheme are summarized. In Appendix B, computational details used in this paper are described. In Appendixes C and D, we detail the corrections used in Secs. II and VI. In Appendix E, we discuss in detail the P dependence at the intermediate stage of the present procedure. In Appendix F, we detail the dependence of AB LEH parameters on crystal parameters (CPs) around optimal pressure.

II. OVERVIEW

The main results obtained in this paper are summarized as (I) and (II) below.

(I) $|t_1^{avg}|$ increases with P . This increase in $|t_1|$ is caused specifically by the uniaxial pressure P_a , in agreement with previous experimental studies on, e.g., Hg1201 [17].

(II) u^{avg} decreases with P . The decrease in u is caused mainly by (I), namely, by the increase in $|t_1|$, but is slowed by the increase in U at $P < P_{opt}$. The increase in U is also caused by P_a .

The nontrivial pressure dependence of T_c^{opt} can be understood from (I) and (II), which is derived from our *ab initio*

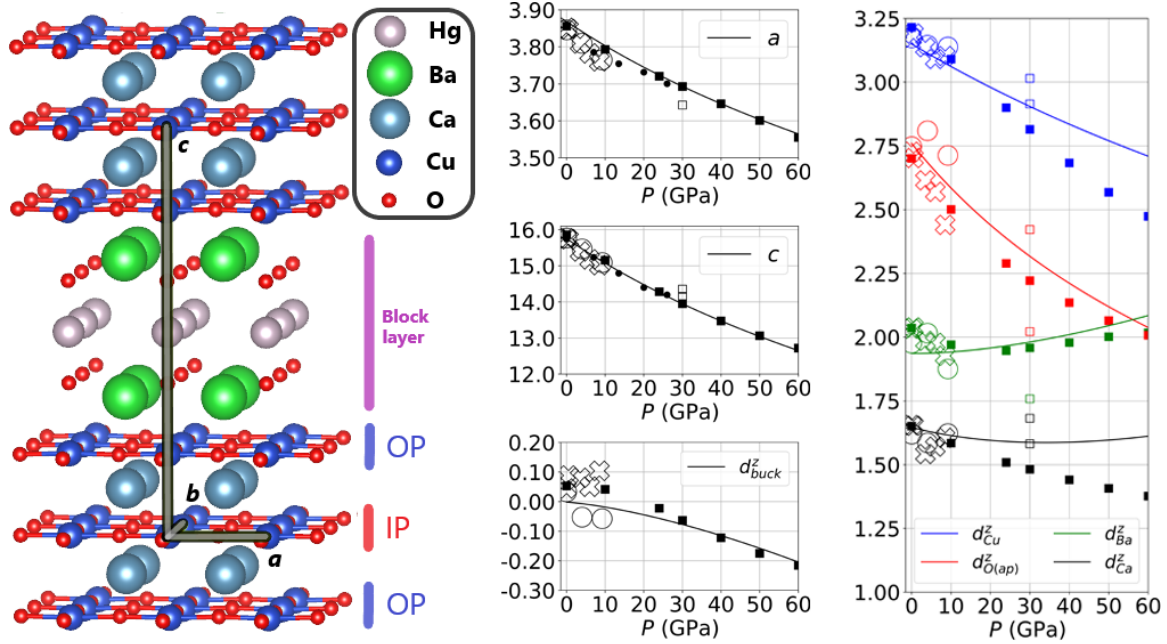


FIG. 2. Left panel: Crystal structure of Hg1223. We show the block layer, the inner CuO₂ plane (IP), the outer CuO₂ plane (OP), and the interstitial Ca atoms. The thick gray lines represent the primitive lattice vectors \mathbf{a} , \mathbf{b} , \mathbf{c} . The cell parameters are $a = |\mathbf{a}| = |\mathbf{b}|$ and $c = |\mathbf{c}|$; other CPs are defined in Table I. Middle and right panels: Pressure dependence of the CP values in Å. We show the optimized CP values (squares) and the extrapolated CP values from Zhang *et al.* [33] (solid lines); for details, see Appendix B 1. The open squares show the modifications of the optimized CP values at $P_{opt} = 30$ GPa that are considered in Appendix F. For comparison, we also show the experimental CP values from Armstrong *et al.* [34] (open crosses) and Hunter *et al.* [35] (open circles), and the values of a and c from Eggert *et al.* [36] (dots).

Hamiltonian even at the preliminary level GGA+cRPA, if we assume the following (A) and (B). [The reality of (A) and (B) will be discussed later in Sec. VI.]

(A) The universal scaling for T_c^{opt} given theoretically as

$$T_c^{est} \simeq 0.16|t_1|F_{SC} \quad (1)$$

recently proposed for the cuprates with $N_\ell = 1, 2$, and ∞ [7,30] is also valid for Hg1223 with $N_\ell = 3$.

(B) F_{SC} follows a universal u dependence revealed in Ref. [7], where F_{SC} has a peak at $u = u_{opt} \simeq 8.0\text{--}8.5$. In addition, at P_{amb} , Hg1223 is located at slightly strong coupling side $u \gtrsim u_{opt}$, while the highest pressure $P = 60$ GPa applied so far is in the weak coupling side $u < u_{opt}$. In fact, we justify later $u \simeq u_{opt}$ at optimal pressure $P_{opt} \simeq 30$ GPa for Hg1223.

To understand the consequences of the assumptions (A) and (B) appropriately and to complement the consequences quantitatively, we correct the errors anticipated in our *ab initio*

GGA+cRPA calculation using the following (C) and (D). [Details of (C) and (D) are given in Appendixes C and D, respectively.]

(C) We correct the values of u^{avg} and $|t_1^{avg}|$ obtained at the GGA+cRPA level by deducing the most sophisticated cGW-SIC+LRFB level. Since GGA+cRPA is known to underestimate u in Bi2201 and Bi₂Sr₂CaCu₂O₈ (Bi2212), it is desirable to improve the AB LEH to the more accurate cGW-SIC+LRFB level. However, the explicit calculation at the cGW-SIC+LRFB level is computationally demanding, while the corrections from the explicitly calculated cGW-SIC to the cGW-SIC+LRFB levels are known to be small and are relatively materials insensitive. Thus we represent the correction by a universal constant with admitted uncertainty. The estimates of u and $|t_1|$ improved in such ways are denoted as $u_{cGW-SIC+LRFB}$ and $|t_1|_{cGW-SIC+LRFB}$. The procedure consists in the two steps (C1) and (C2):

TABLE I. Irreducible Cartesian atomic coordinates (x, y, z) within the unit cell given by the ($\mathbf{a}, \mathbf{b}, \mathbf{c}$) frame in Fig. 2. The atom index l is either Cu(i) (Cu atom in the IP), O(i) (O atom in the IP), Cu(o) (Cu atom in the OP), O(o) (O atom in the OP), O(ap) (apical O atom), Ca, Ba, or Hg. The coordinates of other atoms in the unit cell may be deduced by applying the transformations (y, x, z) to O(i) and O(o) and ($x, y, -z$) to Cu(o), O(o), Ca, Ba, and O(ap). The atomic coordinates are entirely determined by the seven CPs $a, c, d_{Ca}^z, d_{Cu}^z, d_{buck}^z, d_{Ba}^z$, and $d_{O(ap)}^z$. Note that d_{buck}^z [the displacement of O(o) due to the Cu(o)-O(o)-Cu(o) bond buckling] may be either positive or negative. The CP values are listed in Fig. 2 as a function of P .

Atom index l	Cu(i)	O(i)	Ca	Cu(o)	O(o)	Ba	O(ap)	Hg
x	0	$a/2$	$a/2$	0	$a/2$	$a/2$	0	0
y	0	0	$a/2$	0	0	$a/2$	0	0
z	0	0	d_{Ca}^z	d_{Cu}^z	$d_{Cu}^z - d_{buck}^z$	$d_{Cu}^z + d_{Ba}^z$	$d_{Cu}^z + d_{O(ap)}^z$	$c/2$

(C1) cGW-SIC calculation: Starting from the whole and detailed pressure dependence of u^{avg} and $|t_1^{\text{avg}}|$ for Hg1223 calculated at the GGA+cRPA level, we calculate explicitly the level of the cGW-SIC denoted as $u_{\text{cGW-SIC}}$ and $|t_1|_{\text{cGW-SIC}}$ in limited cases of pressure choices of Hg1223 to reduce the computational cost.

(C2) Estimate at the cGW-SIC+LRFB level: We use

$$u_{\text{cGW-SIC+LRFB}} = x_{\text{LRFB}} u_{\text{cGW-SIC}} \quad (2)$$

and

$$|t_1|_{\text{cGW-SIC+LRFB}} = y_{\text{LRFB}} |t_1|_{\text{cGW-SIC}} \quad (3)$$

and estimate constants x_{LRFB} and y_{LRFB} in Hg1223 from the already explicitly calculated results for other compounds Hg1201, CaCuO₂, Bi2201, and Bi2212. The estimated values are $x_{\text{LRFB}} = 0.95$ (with the range of uncertainty 0.91–0.97) and $y_{\text{LRFB}} = 1.0$. See Appendix C for detailed procedure to estimate x_{LRFB} and y_{LRFB} for the case of Hg1223. The concrete effect of (C) for Hg1223 is to increase u from the cRPA level by the ratio $u_{\text{cGW-SIC+LRFB}}/u^{\text{avg}} \simeq 1.29$ at P_{amb} , $\simeq 1.15$ at 30 GPa, and $\simeq 1.08$ at 60 GPa; also, the $\simeq 13\%$ – 14% increase in $|t_1^{\text{avg}}|$ from P_{amb} to 30 GPa becomes $\simeq 17\%$ by this correction.

(D) After applying (C), we further correct the value of $|t_1|_{\text{cGW-SIC+LRFB}}$ by considering the plausible error in crystal parameters at high pressure. Structural optimization by *ab initio* calculation is known to show quantitative error and it is preferable to correct it if experimental value is known. We compare our structural optimization and the experimental cell parameter a if it is available (this is the case at $P < 8.5$ GPa) and assume that this trend of the deviation continues for $P > 8.5$ GPa, where experimental data are missing. Namely, at $P > 8.5$ GPa, we assume that our calculation overestimates the experimental a by $\simeq 0.05$ Å, and we correct a by $\Delta a = -0.05$ Å accordingly. The concrete effect of (D) is that the increase in $|t_1|_{\text{cGW-SIC+LRFB}}$ from P_{amb} to 30 GPa is now $\simeq 22\%$.

The final estimates of $u_{\text{cGW-SIC+LRFB}}$ and $|t_1|_{\text{cGW-SIC+LRFB}}$ are shown in Fig. 1(a). Since (C1) is computationally demanding, we perform (C) and (D) only at P_{amb} , 30 GPa and 60 GPa, and infer the correction at other pressures by linear interpolation for the pressure dependence.

Even by considering only (A) and (B) above, the present mechanism qualitatively accounts for the microscopic trend of the dome structure: At $P < P_{\text{opt}}$, (I), namely, the increase in $|t_1|$, plays the role to increase T_c , whereas the decrease in u does not appreciably affect F_{SC} and thus T_c , because F_{SC} passes through the broad peak region in the u dependence. At $P > P_{\text{opt}}$, (II), namely the decrease in u , drives the decrease in F_{SC} and thus T_c surpassing the increase in $|t_1|$, which generates a dome structure. If we take into account (C) and (D) in addition to (A) and (B), the dome structure in the P dependence of experimental T_c^{opt} is more quantitatively reproduced (see Fig. 1). In addition to the above results, we discuss the dependence of AB LEH parameters on each CP, which provides us with hints for future designing of even higher T_c^{opt} materials.

TABLE II. Definitions of the uniform pressure P and uniaxial pressures P_a , P_c , P_a^{buck} , and P_c^{buck} considered in this paper. Each CP is marked with a check mark if its value is modified by the application of the pressure, and with a cross if not. If the CP value is modified, the value is that in the P dependence in Fig. 2. If not, the value is that at P_{amb} in Fig. 2.

	P	P_a	P_a^{buck}	P_c	P_c^{buck}
a	✓	✓	✓	×	×
d_{buck}^z	✓	×	✓	✓	×
$c, d_{\text{Ca}}^z, d_{\text{Cu}}^z, d_{\text{Ba}}^z, d_{\text{O(ap)}}^z$	✓	×	×	✓	✓

III. FRAMEWORK OF METHOD

We start from the crystal structure of Hg1223 and the pressure dependence of the CP values in Fig. 2. We abbreviate the inner and outer CuO₂ planes shown in Fig. 2 as IP and OP, respectively. The crystal structure is entirely determined by the seven CPs defined in Table I, which consist of the two cell parameters a and c and the five characteristic distances d_i^z . The CP values considered in this paper are listed in Fig. 2, as a function of P . In the main analyses of this paper, we consider (i) CP values obtained by a structural optimization, which are denoted as optimized CP values. For comparison, we also consider (ii) the theoretical calculation of the CP values in Zhang *et al.* [33] for the region between P_{amb} and 20 GPa, and extrapolate the pressure dependence up to 60 GPa. Details about (i) and (ii) are given in Appendix B 1. We also consider (iii) the experimental CP values from Armstrong *et al.* [34] between P_{amb} and 8.5 GPa. (The values at P_{amb} correspond to the SC phase with the experimental SC transition temperature $T_c^{\text{exp}} \simeq 135$ K close to $T_c^{\text{opt}} \simeq 138$ K.) It is known that the optimized CP values slightly deviate from the experimental values, and it is indeed seen in Fig. 2. From the comparison of the optimized and experimental CPs, we take into account the correction (D) addressed in Sec. I.

We simulate at the experimental optimal hole concentration p , which allows a reliable comparison with the P dependence of T_c^{opt} [3]. We use the same procedure as that in Ref. [30] employed for Hg1201: We partially substitute Hg by Au. We consider the chemical formula $\text{Hg}_{1-x_s}\text{Au}_{x_s}\text{Ba}_2\text{Ca}_2\text{Cu}_3\text{O}_8$ with $x_s = 0.6$ in order to realize the average hole concentration per CuO₂ plane $p_{\text{av}} = 0.2$ [5,37,38]. This choice is discussed and justified in Appendix B 2.

In addition, we examine the distinct effects of the uniaxial pressures along axis **a** and axis **c**, whose definitions are given in Table II and discussed below. The nontrivial point is: Experimentally, what are the variations in CP values when the crystal structure is compressed along **a** (**c**)? First, the compression along **a** obviously modifies the cell parameter a as well as the amplitude $|d_{\text{buck}}^z|$ of the Cu-O-Cu bond buckling in the OP, but it should not affect the other CPs $d_{\text{Cu}}^z, d_{\text{Ca}}^z, d_{\text{Ba}}^z$, and $d_{\text{O(ap)}}^z$. Thus, we define the uniaxial pressure P_a^{buck} along **a** as follows: The compression along **a** modifies the values of a and d_{buck}^z , and all other CP values are those at P_{amb} . We also consider a simplified definition, denoted as P_a : The compression along **a** modifies only the value of a , and all other CP values are those at P_{amb} . As we will see, P_a is sufficient to describe the main effect of the compression along **a**. Second,

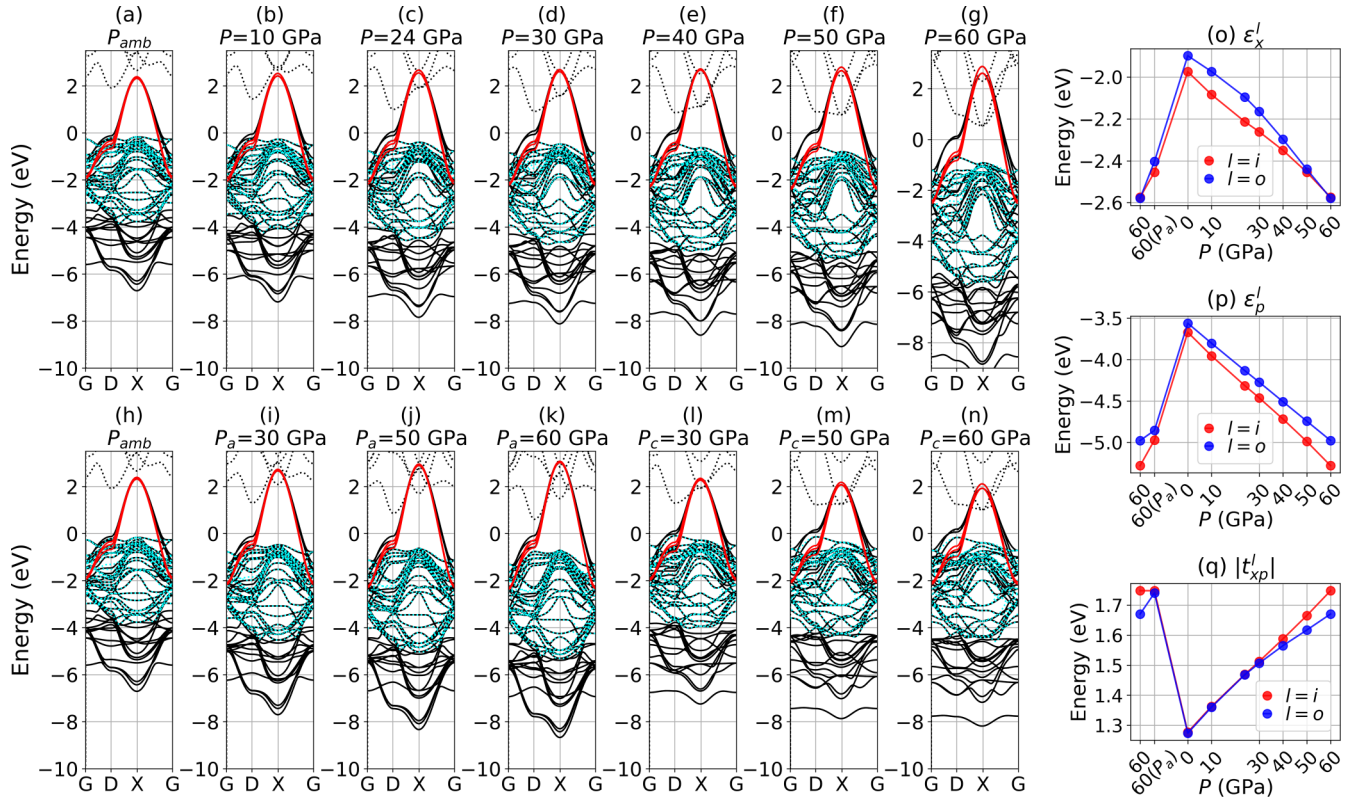


FIG. 3. (a)–(g) Uniform pressure dependence of the GGA band structure. We show the GGA bands outside (dashed black color) and inside (solid black color) the M space, the AB bands (red color), and the 29 other bands in the band window, which are disentangled from the AB band (dashed cyan color). High-symmetry points are, in coordinates of the reciprocal lattice: G = [0 0 0], D = [1/2 0 0], and X = [1/2 1/2 0]. (h)–(n) Uniaxial pressure dependence of the GGA band structure. (o)–(q) Uniform pressure dependence of the $\text{Cu}3d_{x^2-y^2}$ onsite energy ϵ_x^l , the in-plane $O2p_\sigma$ onsite energy ϵ_p^l , and the $\text{Cu}3d_{x^2-y^2}/O2p_\sigma$ hopping in the unit cell t_{xp}^l in the IP ($l = i$) and OP ($l = o$). We also show the result at the uniaxial pressure $P_a = 60$ GPa [denoted as $60(P_a)$]. All quantities are obtained using the optimized CP values.

the compression along \mathbf{c} modifies the values of d_i^z , that is, all CP values except that of a . This uniaxial pressure is denoted as P_c . For completeness, we also consider a second definition, denoted as P_c^{buck} : The compression along \mathbf{c} modifies all CP values except those of a and d_{buck}^z . This allows to discuss the effect of the relatively large value of $|d_{\text{buck}}^z|$ at $P > P_{\text{opt}}$. In the main analyses of this paper, we consider P_a (P_c) to simulate the compression along \mathbf{a} (\mathbf{c}). We also give complementary results by considering P_a^{buck} and P_c^{buck} .

We first compute the electronic structure at the DFT level. The P dependence of the GGA band structure is demonstrated in Fig. 3, from which we derive the LEH spanned by the $\text{Cu}3d_{x^2-y^2}/O2p_\sigma$ AB bands by employing the GGA+cRPA scheme sketched in Appendix A. Computational details of DFT and GGA+cRPA scheme are described in Appendix B.

Then, we define the AB LEH as follows. In the AB LEH for multilayer cuprates [30], there is only one AB orbital centered on each Cu atom. Then the AB LEH reads

$$\mathcal{H} = \sum_{l,l'} \mathcal{H}^{l,l'} = \sum_{l,l'} [\mathcal{H}_{\text{hop}}^{l,l'} + \mathcal{H}_{\text{int}}^{l,l'}], \quad (4)$$

where $l, l' = \{i, o, o'\}$ with i being an IP site, and o, o' belonging to the two equivalent OPs. In which we distinguish

the hopping and interaction parts between planes l and l' , as, respectively,

$$\mathcal{H}_{\text{hop}}^{l,l'} = \sum_{(\sigma\mathbf{R}), (\sigma'\mathbf{R}')} t^{l,l'}(\mathbf{R}' - \mathbf{R}) \hat{c}_{l\sigma\mathbf{R}}^\dagger \hat{c}_{l'\sigma'\mathbf{R}'}, \quad (5)$$

$$\mathcal{H}_{\text{int}}^{l,l'} = \sum_{(\sigma\mathbf{R}), (\sigma'\mathbf{R}')} U^{l,l'}(\mathbf{R}' - \mathbf{R}) \hat{n}_{l\sigma\mathbf{R}} \hat{n}_{l'\sigma'\mathbf{R}'}, \quad (6)$$

where σ, σ' are the spin indices. By using these notations, $(l\sigma\mathbf{R})$ is the AB spin orbital in the plane l and in the unit cell at \mathbf{R} , with spin σ . $c_{l\sigma\mathbf{R}}^\dagger$, $c_{l\sigma\mathbf{R}}$, and $\hat{n}_{l\sigma\mathbf{R}}$ are, respectively, the creation, annihilation, and number operators in $(l\sigma\mathbf{R})$, and $t^{l,l'}(\mathbf{R}' - \mathbf{R})$ and $U^{l,l'}(\mathbf{R}' - \mathbf{R})$ are, respectively, the hopping and direct interaction parameters between $(l\sigma\mathbf{R})$ and $(l'\sigma'\mathbf{R}')$. The translational symmetry allows us to restrict the calculation of LEH parameters to $t_{\sigma,\sigma'}^{l,l'}(\mathbf{R})$ and $U_{\sigma,\sigma'}^{l,l'}(\mathbf{R})$ between $(l\sigma\mathbf{0})$ and $(l'\sigma'\mathbf{R})$.

In this paper, we focus on the intraplane LEH $\mathcal{H}^l = \mathcal{H}^{l,l}$ within the plane l and analyze only the first nearest-neighbor hopping $t_1^l = t^{l,l}([100])$ and the onsite effective interaction $U^l = U^{l,l}([000])$, because these two parameters were proposed to essentially determine T_c^{opt} at least for single- and two-layer cuprates [7]. (Other LEH parameters are given in the Supplemental Material [32].) Then within this restricted

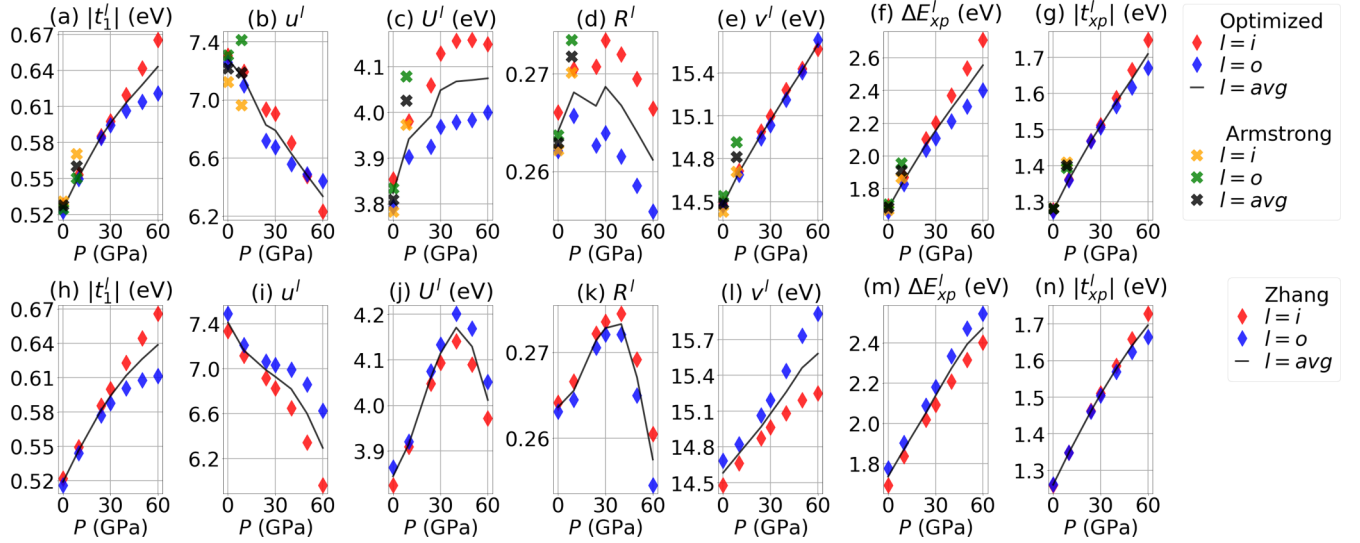


FIG. 4. Uniform pressure dependence of the AB LEH parameter values in the IP ($l = i$), the OP ($l = o$), and the average value over the IP and OP ($l = \text{avg}$). We show the basic energy unit $|t_1^l|$, the correlation strength $u^l = U^l/|t_1^l|$, the onsite effective Coulomb interaction U^l , the screening ratio $R^l = U^l/v^l$, and the onsite bare interaction v^l . In addition, we show the charge transfer energy ΔE_{xp}^l , and the amplitude of the hopping t_{xp}^l between the $\text{Cu}3d_{x^2-y^2}$ and in-plane $\text{O}2p_\sigma$ ALWOs at the GGA level. We show the quantities obtained using the optimized CP values (a)–(g), the experimental CP values from Armstrong *et al.* [34] at P_{amb} and 8.5 GPa [crosses in (a)–(g)], and the CP values from Zhang *et al.* (h)–(n).

range, \mathcal{H}^l is rewritten as

$$\mathcal{H}^l = |t_1^l|[\tilde{\mathcal{H}}_{\text{hop}}^l + u^l \tilde{\mathcal{H}}_{\text{int}}^l] = |t_1^l| \tilde{\mathcal{H}}^l, \quad (7)$$

in which $\tilde{\mathcal{H}}_{\text{hop}}^l = \mathcal{H}_{\text{hop}}^l/|t_1^l|$ and $\tilde{\mathcal{H}}_{\text{int}}^l = \mathcal{H}_{\text{int}}^l/U^l$ are the dimensionless hopping and interaction parts, expressed in units of their respective characteristic energies $|t_1^l|$ and U^l . The full dimensionless intraplane LEH is $\tilde{\mathcal{H}}^l = \mathcal{H}^l/|t_1^l|$, and the dimensionless ratio $u^l = U^l/|t_1^l|$ encodes the correlation strength. As mentioned in Sec. I, we also discuss the values of $|t_1^{\text{avg}}| = (|t_1^i| + |t_1^o|)/2$ and $u^{\text{avg}} = (u^i + u^o)/2$. Average values of other quantities with the superscript l are defined similarly.

We compute the above LEH parameters $|t_1^l|$ and U^l as follows. We use the RESPACK code [30,39]. The standard calculation procedure is presented in detail elsewhere [30,39]. First, we compute t_1^l as

$$t_1^l = \int_{\Omega} dr w_{i0}^*(r) h(r) w_{l\mathbf{R}_1}(r), \quad (8)$$

in which $w_{l\mathbf{R}}$ is the Wannier function of the AB orbital ($l\mathbf{R}$), $\mathbf{R}_1 = [100]$, Ω is the unit cell, and h is the one-particle part at the GGA level. Then we compute U^l as follows. We compute the cRPA effective interaction W_{H} , whose expression is found in Appendix B 5, Eq. (B6). We use a plane wave cutoff energy of 8 Ry. We deduce the onsite effective Coulomb interaction as

$$U^l = \int_{\Omega} dr \int_{\Omega} dr' w_{i0}^*(r) w_{i0}^*(r') W_{\text{H}}(r, r') w_{i0}(r) w_{i0}(r'). \quad (9)$$

We also deduce the onsite bare Coulomb interaction v^l by replacing W_{H} by the bare Coulomb interaction v in Eq. (9), and the cRPA screening ratio $R^l = U^l/v^l$. The obtained values of $|t_1^l|$, U^l , v^l and R^l are plotted in Fig. 4.

IV. PRESSURE DEPENDENCE OF ELECTRONIC STRUCTURE AT DFT LEVEL

Now, we show the result of GGA calculation as a function of P and clarify what can be learned within the DFT level already. The band dispersion is shown in Figs. 3(a)–3(l). We also show in Figs. 3(o)–3(q) the onsite energy of the $\text{Cu}3d_{x^2-y^2}$ and in-plane $\text{O}2p_\sigma$ atomiclike Wannier orbital (ALWO). (As explained in Appendix B, we denote these ALWOs as M-ALWOs because they are in the M space.) We also show the $\text{Cu}3d_{x^2-y^2}/\text{O}2p_\sigma$ hopping amplitude $|t_{xp}^l| = |t_{x^2-y^2, p_\sigma}^{\text{Cu}(l), \text{O}(l)}|$ in the unit cell.

We first elucidate main mechanisms of the following items [MW], [M ϵ], and [Mt] when P increases:

[MW] Broadening of the M band dispersion in Figs. 3(a)–3(g)

[M ϵ] Decrease in onsite energies of M-ALWOs relative to the Fermi level in Figs. 3(o) and 3(p).

[Mt] Increase in hoppings between M-ALWOs in Fig. 3(q).

A simple interpretation of [MW], [M ϵ], and [Mt] is that P works to reduce the interatomic distances. This causes two distinct effects: First, the electrons in the CuO_2 plane feel the stronger Madelung potential from ions in the crystal. Indeed, the amplitude of the Madelung potential scales as $1/d$, where d is the interatomic distance between the ion and the Cu or O atom in the CuO_2 plane. The variation in Madelung potential modifies the M-ALWO onsite energies and causes [M ϵ] (for details, see Appendix E 1). Second, the overlap and hybridization between M-ALWOs increases, which causes [Mt]. Both [M ϵ] and [Mt] increase the splitting of the B/NB (bonding/nonbonding) and AB bands, which causes [MW]: The bandwidth W of the M bands increases from $W \simeq 9$ eV at P_{amb} to $W \simeq 12$ eV at $P = 60$ GPa [see Figs. 3(a)–3(g)]. Simultaneously, the bandwidth W_{AB} of the AB band increases

TABLE III. Summary of the variations in AB LEH parameters with $P < P_{\text{opt}}$ and $P > P_{\text{opt}}$ in Fig. 4. We use \nearrow , $\nearrow\uparrow$, \simeq , \searrow , or $\searrow\downarrow$ if the quantity increases, strongly increases, remains static, decreases, or strongly decreases, respectively. The variation in $u = U/|t_1|$ is controlled by that in $|t_1|$ and U . The variation in $U = vR$ is controlled by that in the onsite bare interaction v and the cRPA screening ratio R .

	$ t_1 $	$u = U/ t_1 $	$U = vR$	v	R
$P < P_{\text{opt}}$	$\nearrow\uparrow$	\searrow	\nearrow	\nearrow	\nearrow
$P > P_{\text{opt}}$	$\nearrow\uparrow$	$\searrow\downarrow$	\simeq / \searrow	\nearrow	$\searrow / \searrow\downarrow$

from $W_{\text{AB}} \simeq 4$ eV at P_{amb} to $W_{\text{AB}} \simeq 5.5$ eV at $P = 60$ GPa, which is caused by $[Mt]$. Indeed, the increase in $|t_1^l|$ and thus $W_{\text{AB}} \simeq 8|t_1^l|$ originates from the increase in $|t_{xp}^l|$, as discussed later in Sec. V A.

Effects of the uniaxial pressures P_a and P_c to $[MW]$, $[M\epsilon]$, and $[Mt]$ can also simply be accounted for when we consider the anisotropy of the overlap of the two M-ALWOs and the direction of the pressure. For instance, $[MW]$ is caused by P_a rather than P_c [see Figs. 3(h)–3(n)], because the AB bandwidth W_{AB} and W are mainly determined by the overlap between $\text{Cu}3d_{x^2-y^2}$ and $\text{O}2p_\sigma$ ALWOs in a CuO_2 plane. This increase in the bandwidth with P_a was also mentioned in Ref. [40] in the case of $\text{Hg}1201$. On the other hand, the application of P_c shifts a few specific bands: $\text{Hg}5d$ -like bands are shifted from $-4/-5$ eV at P_{amb} to -7 eV at $P_c = 30$ GPa. However, P_c does not modify W_{AB} . Effects of uniaxial pressure on $[M\epsilon]$ and $[Mt]$ are also obviously and intuitively understood in a similar fashion: We clearly see in Figs. 3(o)–3(q) that $[M\epsilon]$ and $[Mt]$ are caused by P_a rather than P_c . For more details of the pressure effects, see Appendix E 1.

V. PRESSURE DEPENDENCE OF AB EFFECTIVE HAMILTONIAN

Now, we discuss the P dependence of AB LEH parameters in Figs. 4(a) and 4(b), in which the two main mechanisms

(I, II) are visible: (I) $|t_1^l|$ increases, whereas (II) u^l decreases. In this section, we discuss the mechanisms of (I) and (II) that are summarized in Table III, and demonstrate that (I) and (II) are indeed physical and robust. We discuss mainly $|t_1^{\text{avg}}|$ and u^{avg} , and discuss briefly the difference between values in the IP and OP. A comparison with experiments will be made separately in Sec. VI.

A. Increase in $|t_1|$ with P

The increase (I) in the P dependence of $|t_1^{\text{avg}}|$ [see Fig. 4(a)] is purely caused by the reduction of cell parameter a when the crystal is compressed along axis \mathbf{a} . Indeed, (I) is purely caused by the application of P_a [see Fig. 5(a)], whose only effect is to reduce a . The underlying origin is simply the increase in overlap between AB orbitals on neighboring Cu atoms due to the decrease in cell parameter a when increasing P_a as already discussed in Sec. IV at the DFT level. We note that $|t_1^l|$ has a similar P dependence as that of $|t_{xp}^l|$ [see Figs. 4(a) and 4(g)]. This is obvious because the AB orbital is formed by the hybridization of $\text{Cu}3d_{x^2-y^2}$ and $\text{O}2p_\sigma$ M-ALWOs.

Note that, at $P > P_{\text{opt}}$, $|t_1^o|$ is reduced with respect to $|t_1^i|$; this is because of the buckling of Cu-O-Cu bonds in the OP. Indeed, the decrease in $|t_1^o| - |t_1^i|$ and also $|t_{xp}^o| - |t_{xp}^i|$ occurs in the P_a^{buck} dependence [see Fig. 5(h)] but not in the P_a dependence [see Fig. 5(a)], and the value of d_{buck}^z is modified by the application of P_a^{buck} but not by the application of P_a . Furthermore, the P dependence of $|t_1^o| - |t_1^i|$ is consistent with that of $|d_{\text{buck}}^z|$: The decrease in $|t_1^o| - |t_1^i|$ starts at P_{opt} and is amplified at larger pressures [see Figs. 4(a) and 4(g)], which is consistent with the increase in $|d_{\text{buck}}^z|$ from 0.05 Å to 0.20 Å between P_{opt} and 60 GPa (see Fig. 2). The origin of the decrease in $|t_1^o| - |t_1^i|$ can be understood as follows: When $|d_{\text{buck}}^z|$ increases, the overlap between $\text{Cu}3d_{x^2-y^2}$ and $\text{O}2p_\sigma$ M-ALWOs in the OP is reduced. Note that the buckling induced decrease in $|t_1|$ has also been observed in the two-layer cuprate $\text{Bi}2212$ [30].

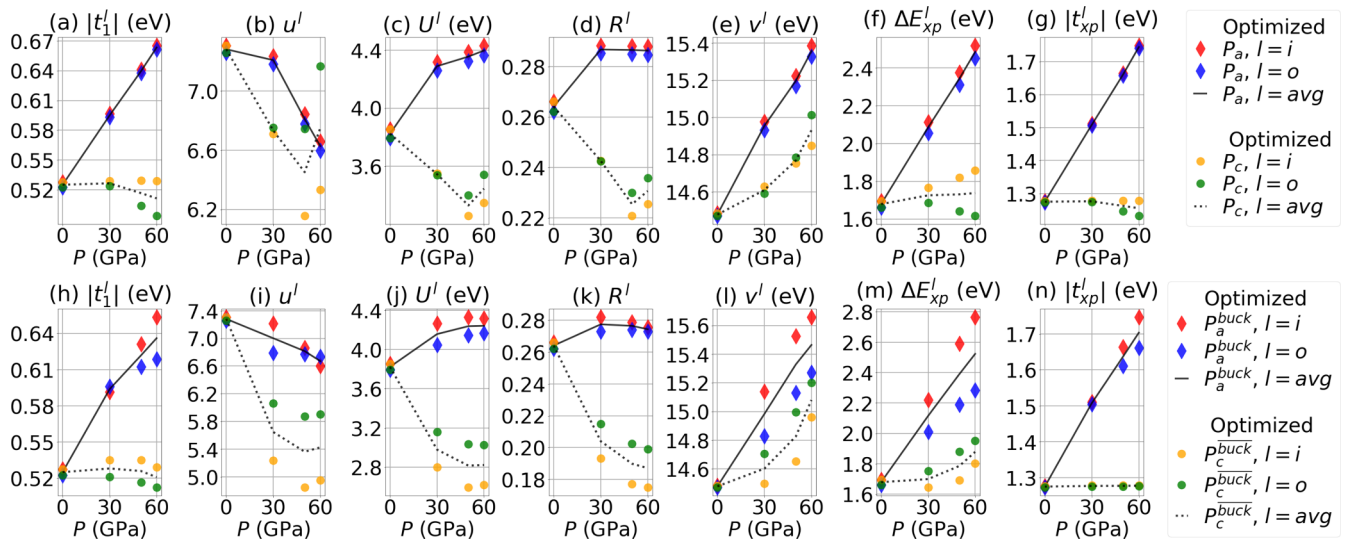


FIG. 5. Uniaxial pressure dependence of the AB LEH parameter values. Notations are the same as those in Fig. 4. All quantities are obtained using the optimized CP values. We show the P_a and P_c dependencies (a)–(g), and the P_a^{buck} and P_c^{buck} dependencies (h)–(n).

Comparison of results obtained from different CP values shows that (I) is physical and robust. If we consider both (i) the optimized CP values and (ii) the CP values from Zhang *et al.*, the P dependencies of $|t_1^l|$ and $|t_{xp}^l|$ are very similar for (i) and (ii) [see Figs. 4(a), 4(g), 4(h), and 4(n)]. This is intuitive since the P dependence of a is similar for (i) and (ii), and the P dependence of d_{buck}^z at $P > P_{\text{opt}}$ is also similar (see Fig. 2). If we consider (iii) the experimental CP values from Armstrong *et al.* [34] at $P < 8.5$ GPa, the increase in $|t_1^{\text{avg}}|$ and $|t_{xp}^{\text{avg}}|$ is faster. This is in accordance with the faster decrease in a for (iii) with respect to (i) and (ii) (see Fig. 2), and implies the uncertainty of the estimate of $|t_1^{\text{avg}}|$ at P_{opt} , as discussed later in Sec. VI.

B. Decrease in u with $P < P_{\text{opt}}$

At $P < P_{\text{opt}}$, the decrease (II) in u^{avg} is largely induced by the increase (I) in $|t_1^{\text{avg}}|$; however, the increase in U^{avg} [see Fig. 4(c)] partially cancels the decrease in u^{avg} . Thus, we discuss the P dependence of U^{avg} below.

The increase in U^{avg} is caused by two cooperative factors (i, ii) whose main origin is the reduction in a . These are (i) the increase in onsite bare interaction v^{avg} [see Fig. 4(c)], and (ii) the reduction in cRPA screening represented by the increase in the average value R^{avg} of the cRPA screening ratio $R^l = U^l/v^l$ [see Fig. 4(d)]. In the following, we discuss the microscopic origins of (i) and (ii).

On (i), the increase in v^l mainly originates from the increase in charge transfer energy ΔE_{xp}^l between $\text{Cu}3d_{x^2-y^2}$ and $\text{O}2p_\sigma$ M-ALWOs. This is because the increase in ΔE_{xp}^l reduces the importance of the $\text{Cu}3d_{x^2-y^2}/\text{O}2p_\sigma$ hybridization. (The latter is roughly encoded in the ratio $O_{xp}^l = |t_{xp}^l|/\Delta E_{xp}^l$.) The reduction in hybridization increases the $\text{Cu}3d_{x^2-y^2}$ atomic character and thus the localization of the AB orbital. This is discussed and justified in item (a) in Appendix E 2. This simple view is consistent with the systematic correlation between v^l and ΔE_{xp}^l in this paper [see Figs. 4(e), 4(f), 4(l), and 4(m)] and Appendix F, and also in the literature [27,30]. Still, note that the correlation between v^l and ΔE_{xp}^l is slightly reduced at $P > P_{\text{opt}}$ [see Figs. 4(e), 4(f), 4(l), and 4(m)] at $P > P_{\text{opt}}$. This is because $|t_{xp}^o|$ is reduced with respect to $|t_{xp}^i|$ at $P > P_{\text{opt}}$ due to the nonzero d_{buck}^z , which contributes to reduce O_{xp}^o [see also item (c) in Appendix E 2].

The increase in ΔE_{xp}^l mainly originates from the reduction in a . Indeed, the increase is mainly caused by P_a [see Fig. 5(f)]. This is because the reduction in a increases the energy of $\text{Cu}3d_{x^2-y^2}$ electrons with respect to that of $\text{O}2p_\sigma$ electrons (see Appendix E 1). Although the reduction in a is the main origin of the increase in the P dependence of $\Delta E_{xp}^{\text{avg}}$, note that ΔE_{xp}^l depends not only on a but also on other CPs (see Appendix F).

The concomitant increases in v^l and $|t_1^l|$ seem counterintuitive but can be explained as follows. The counterintuitive point is that the increase in v^l suggests a more localized AB orbital whereas the increase in $|t_1^l|$ would be more consistent with a delocalization of the AB orbital. Although the AB orbital is more localized, the increase in $|t_1^l|$ is explained by the increase in $|t_{xp}^l|$ with P_a in Fig. 4(g). This is discussed in detail in item (b) in Appendix E 2, which is summarized below. We apply P_a and examine the a dependencies of $|t_1^{\text{avg}}|$,

$|t_{xp}^{\text{avg}}|$, and $\Delta E_{xp}^{\text{avg}}$, and the average values O_{xp}^{avg} and T_{xp}^{avg} of O_{xp}^l and $T_{xp}^l = |t_{xp}^l|^2/\Delta E_{xp}^l$. The increase in $\Delta E_{xp}^{\text{avg}}$ with a is faster than the increase in $|t_{xp}^{\text{avg}}|$, but slower than the increase in $|t_{xp}^{\text{avg}}|^2$. As a result, when a decreases, $|t_1^{\text{avg}}| \propto T_{xp}^{\text{avg}} \propto 1/a^3$ increases. On the other hand, $O_{xp}^{\text{avg}} \propto a$ decreases, hence the increase in v^l .

On (ii), the decrease in cRPA screening [the increase in R^l in Fig. 4(d)] is due to the broadening [MW] of the GGA band dispersion (whose origin is the reduction in a as discussed in Sec. IV). Indeed, [MW] causes the increase in charge transfer energies between occupied bands and empty bands, which reduces the amplitude of the cRPA polarization (see Appendix E 3 for details). The increase in R^l is monotonous, except for the small dip in the P dependence of R^o at $P \simeq 24$ GPa in Fig. 4(d). The dip may originate from the change in the sign of d_{buck}^z at $P \simeq 24$ GPa (see the next paragraph).

Comparison of results obtained from different CP values shows that (i) and (ii) are essentially correct, independently of the uncertainty on CP values. Let us consider the results obtained from the CP values from Zhang *et al.* in Figs. 4(h)–4(n) and compare them with the results obtained from the optimized CP values in Figs. 4(a)–4(g). The increase in v^{avg} is well reproduced [see Figs. 4(e) and 4(l)]. The increase in R^{avg} with P is qualitatively reproduced [see Figs. 4(d) and 4(k)]; however, the P dependence of R^l is not exactly the same, and we discuss the difference below.

First, there is a small dip in the P dependence of R^o at $P \simeq 24$ GPa in Fig. 4(d) (optimized CP values). This dip is not observed in Fig. 4(k) (CP values from Zhang *et al.*). This may be because the sign of d_{buck}^z does not change at $P \simeq 24$ GPa if we consider the CP values from Zhang *et al.*, contrary to the optimized CP values (see the P dependence of d_{buck}^z in Fig. 2).

Second, at $P_{\text{opt}} = 30$ GPa, the value of R^l is similar but the value of R^o is larger in Fig. 4(k) with respect to Fig. 4(d). This is because the values of both d_{Ca}^z and d_{Cu}^z are larger in Zhang *et al.* with respect to the optimized CP value (the difference is 0.1 Å as seen in Fig. 2). As shown in Appendix F, the larger value of d_{Ca}^z increases R^o . At the same time, the larger value of d_{Cu}^z decreases (increases) R^l . (Both effects cancel each other.)

Finally, if we consider the experimental CP values from Armstrong *et al.*, the increases (i) and (ii) are faster [see Figs. 4(d) and 4(e)]. This is consistent with the faster decrease in a in Armstrong *et al.* with respect to the optimized CP values and those from Zhang *et al.* (see Fig. 2).

C. Decrease in u with $P > P_{\text{opt}}$

At $P > P_{\text{opt}}$, the decrease in u^{avg} is faster because R^{avg} decreases. Let us start from the P dependence of U^{avg} : At $P > P_{\text{opt}}$, U^{avg} ceases to increase [see Fig. 4(c)] and may even decrease if we consider the CP values from Zhang *et al.* [see Fig. 4(i)]. The origin is not the P dependence of v^{avg} , which increases monotonically [see Figs. 4(e) and 4(l)], but rather that of R^{avg} , which shows a dome structure with a maximum at $P_{\text{scr}} \simeq 30$ –40 GPa and a decrease at $P > P_{\text{scr}}$ [see Figs. 4(d) and 4(k)]. The decrease in R^{avg} dominates the increase in v^{avg} .

The decrease in R^{avg} looks physical, and robust with respect to the uncertainty on CP values. It is still observed

if we consider the CP values from Zhang *et al.* instead of the optimized CP values [see Fig. 5(k)], even though the P dependence of R^l is modified.

The decrease in R^{avg} is the result of a competition between P_a and P_c . (The effect of P_c is dominant at $P > P_{\text{opt}}$.) As seen in Fig. 5(d), applying only P_a causes (i) the nonlinear increase in R^{avg} , which dominates at $P < P_{\text{opt}}$ but saturates at $P > P_{\text{opt}}$. On the other hand, applying only P_c causes (ii) the decrease in R^{avg} , which becomes dominant at $P > P_{\text{opt}}$. [(i) and (ii) are interpreted in terms of the cRPA polarization in Appendix E.3.] The microscopic origin of (ii) is the decrease in both d_{Cu}^z and $d_{\text{O(ap)}}^z$ when P_c is applied (see Appendix F).

Note that, in the OP, the destructive effect of P_c on R^o and thus u^o is canceled by the buckling induced decrease in $|t_1^o|$. Indeed, the P_c dependence of u^o in Fig. 5(b) shows a 6% increase from P_{opt} to 60 GPa. This increase originates from the buckling of Cu-O-Cu bonds in the OP, because it does not appear in the P_c^{buck} dependence of u^o in Fig. 5(i), and the value of d_{buck}^z is modified by applying P_c but not by applying P_c^{buck} . The buckling reduces $|t_1^o|$ as discussed in Sec. V A, which is the main origin of the increase in u^o from P_{opt} to 60 GPa.

VI. DISCUSSION

Here we discuss in detail how the experimental P dependence of T_c^{opt} is predicted by considering (I) and (II) together with the assumptions (A, B) and the corrections (C, D) in Sec. I. We also discuss that (A) through (D) are all physically sound.

First, we emphasize that only by considering (A) and (B), the dome structure in the P dependence of T_c^{opt} is qualitatively understood. Since (B) implies that F_{SC} stays at a plateau region around the peak of parabolic P dependence between P_{amb} and P_{opt} as is seen in Fig. 1(a). Then the dominant P dependence of F_{SC} arises from t_1 , which causes an increase in T_c^{est} in Eq. (1). On the other hand, F_{SC} rather rapidly decreases with increasing P above P_{opt} , which dominates over the effect of increase in $|t_1|$.

The location of Hg1223 assumed in (B) is justified from (C). Without (C), we would have $u^{\text{avg}} \simeq 7.2$ at P_{amb} and $\simeq 6.8$ at P_{opt} : Both values are below $u_{\text{opt}} \simeq 8.0 - 8.5$, so that F_{SC} would quickly decrease with P , and (B) would not be valid. On the other hand, if we apply (C), we have $u \simeq 9.3 \gtrsim u_{\text{opt}}$ at P_{amb} and $\simeq 7.8 \simeq u_{\text{opt}}$ at P_{opt} [see Fig. 6(a)], so that (B) becomes valid.

Let us discuss more quantitative aspects. Although F_{SC} does not vary substantially with increasing P below P_{opt} , there is a small ($\simeq 5\%$) decrease in F_{SC} from P_{amb} to P_{opt} even after applying (C) [see Fig. 1(a)]. If we apply (C) without (D), the $\simeq 13\% - 14\%$ increase in $|t_1^{\text{avg}}|$ from P_{amb} to P_{opt} becomes the $\simeq 17\%$ increase in $|t_1|$. However, the increase in T_c^{est} estimated from Eq.(1) is only $\simeq 10\%$ due to the $\simeq 5\%$ decrease in F_{SC} . If we apply (D) after (C), the increase in $|t_1|$ becomes $\simeq 22\%$, so that the increase in T_c^{est} becomes $\simeq 17\%$ and reproduces that in T_c^{opt} . Note that the quantitative agreement between the increases in T_c^{est} and T_c^{opt} is very good at $x_{\text{LRFB}}^{\text{est}} = 0.95$ at least for small P [see Fig. 1(b)]. For completeness, note that (D) has a limitation: It relies on the a dependence of $|t_1|$ at the

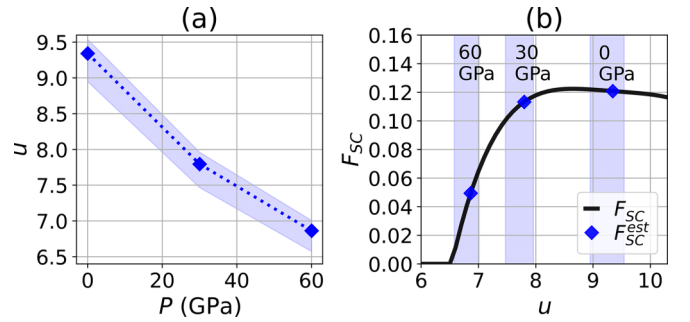


FIG. 6. (a) P dependence of estimated u at the cGW-SIC+LRFB level denoted here as $u_{\text{cGW-SIC+LRFB}}$. The diamond symbols show $u_{\text{cGW-SIC+LRFB}}$ with the choice of $x_{\text{LRFB}} = 0.95$ correcting explicit calculations at the cGW-SIC level employing Eq. (2). The dashed lines show linear interpolations between the diamond symbols. The colored shaded area corresponds to the range $x_{\text{LRFB}} = 0.91 - 0.97$. (b) u dependence of F_{SC} extracted from Schmid *et al.* [7], Fig. 10. We also show $F_{\text{SC}}^{\text{est}}$ at 0, 30 and 60 GPa.

GGA+cRPA level. [For more details, see the last paragraph of Appendix D.]

Now, we argue that (A)–(D) are adequate from the physical point of view. On (A), it was shown that the scaling Eq. (1) is equally satisfied for $N_\ell = 1, 2$ and ∞ [7]. This is on the one hand due to the fact that the interlayer coupling is small for all the cases and within a CuO_2 layer on the other hand, the superconductivity is mainly dependent on t_1 and U only, and the dependence on other parameters is weak within the realistic range. In the present case of Hg1223 with $N_\ell = 3$, the interlayer coupling is again small. For instance, the ratio between the interlayer offsite Coulomb repulsion $V^{i,o}$ and U^{avg} is $V^{i,o}/U^{\text{avg}} = 0.13$ at P_{amb} , and the superconducting strength is expected to be governed by the single-layer physics, which is the same as the cases of $N_\ell = 1, 2$, and ∞ .

On (B), the statement that $u_{\text{cGW-SIC+LRFB}}$ at P_{amb} is above $u_{\text{opt}} \simeq 8.0 - 8.5$ is indeed satisfied in the *ab initio* estimate by considering the correction (C). As mentioned earlier, the GGA+cRPA estimate is $u^{\text{avg}} \simeq 7.2 < u_{\text{opt}}$ at P_{amb} . However, (C) yields $u_{\text{cGW-SIC+LRFB}} \simeq 9.3 \gtrsim u_{\text{opt}}$ at P_{amb} , and $u_{\text{cGW-SIC+LRFB}} \simeq 7.8 \simeq u_{\text{opt}}$ at P_{opt} [see Fig. 6(a)].

On (C), the calculation of $u_{\text{cGW-SIC+LRFB}}$ and $|t_1|_{\text{cGW-SIC+LRFB}}$ is detailed in Appendix C.

On (D), it is plausible that our calculation overestimates a by $\simeq 0.05 \text{ \AA}$ at $P > 8.5$ GPa, because the same overestimation is already observed at $P = 8.5$ GPa in Fig. 2. The derivation of improved $|t_1|_{\text{cGW-SIC+LRFB}}$ is detailed in Appendix D.

In Fig. 1(b), although the pressure dependence of T_c^{opt} is nicely reproduced for $P < P_{\text{opt}}$, the estimated T_c^{est} decreases more rapidly than the experimental T_c^{opt} at $P > P_{\text{opt}}$. The origin of this discrepancy is not clear at the moment. One possible origin is of course the uncertainty of the crystal parameters at high pressure because there exist no experimental data. Another origin would be the limitation of the inference for the LRFB correction taken simply by the constants x_{LRFB} and y_{LRFB} . The third possibility is the possible inhomogeneity of the pressure in the experiments. The complete understanding of the origin of the discrepancy is an intriguing future issue.

VII. SUMMARY AND CONCLUSION

We have proposed the microscopic mechanism for the domelike P dependence of T_c^{opt} in Hg1223 as the consequence of (I) and (II) obtained in this paper together with the assumptions (A, B) and the corrections (C, D) mentioned in Sec. II and supported in Sec. VI. We have also elucidated the microscopic origins of (I) and (II), which are summarized below.

(I) The increase in $|t_1|$ is caused by the reduction in the cell parameter a when the crystal is compressed along axis \mathbf{a} .

(II) The decrease in u is induced by (I), but is partially canceled by the increase in U at $P < P_{\text{opt}}$. The increase in U is caused by two cooperative factors: (i) the increase in onsite bare interaction v , whose main origin is the reduction in $\text{Cu}3d_{x^2-y^2}/\text{O}2p_\sigma$ hybridization, and (ii) the reduction in cRPA screening at $P < P_{\text{opt}}$. Both (i) and (ii) originate from the reduction in a . At $P > P_{\text{opt}}$, U ceases to increase with increasing P , because the cRPA screening increases due to the compression along axis \mathbf{c} , more precisely the reduction in distance d_{Cu}^z between the IP and OP [$d_{\text{O(ap)}}^z$ between the OP and apical O], which screens AB electrons in the IP (OP).

The elucidation of the above mechanisms offers a platform for future studies on cuprates under P and design of new compounds with even higher T_c^{opt} : For instance, T_c may be controlled by controlling $|t_1|$ via the cell parameter a . However, the increase in $|t_1|$ is a double-edged sword for the increase in T_c : On one hand, it is the direct origin of the increase in $T_c^{\text{opt}} \propto |t_1|$ at $P < P_{\text{opt}}$ in Hg1223. On the other hand, it is a prominent cause of the decrease in u and thus F_{SC} and T_c^{opt} at $P > P_{\text{opt}}$. Conversely, in the OP, the buckling of Cu-O-Cu bonds reduces $|t_1|$: This reduces $T_c^{\text{opt}} \propto |t_1|$, but this may also increase F_{SC} and thus T_c^{opt} if the value of u is in the weak-coupling region [$u < 7.5$ in Fig. 6(b)]. For instance, the buckling may be identified as the main origin of the higher T_c^{opt} in Bi2212 ($T_c^{\text{opt}} \simeq 84$ K [2]) compared to Bi2201 ($T_c^{\text{opt}} \simeq 6$ K [2]): The buckling reduces $|t_1|$ and thus increases u in Bi2212 with respect to Bi2201 [30], so that Bi2212 is near the optimal region whereas Bi2201 is in the weak-coupling region [7]. This explains the larger $|t_1|F_{\text{SC}}$ in Bi2212 [7] despite the smaller $|t_1|$.

ACKNOWLEDGMENTS

We thank Michael Thobias Schmid for useful discussions. This work was supported by MEXT as a Program for Promoting Researches on the Supercomputer Fugaku (Basic Science for Emergence and Functionality in Quantum Matter-Innovative Strongly-Correlated Electron Science by Integration of Fugaku and Frontier Experiments, JPMXP1020200104 and JPMXP1020230411) and used computational resources of the supercomputer Fugaku provided by the RIKEN Center for Computational Science (Project IDs hp200132, hp210163, hp220166, and hp230169). We also acknowledge the financial support of JSPS Kakenhi Grant-in-Aid for Transformative Research Areas, Grants No. JP22H05111 and No. JP22H05114 (“Foundation of Machine Learning Physics”). Part of the results were obtained under the Special Postdoctoral Researcher Program at RIKEN. The left panel of Fig. 2 was drawn using software VESTA [41].

APPENDIX A: METHOD OF MACE

Here, as a complement to Sec. I, we summarize and comment the MACE methodology that is used to derive the effective Hamiltonian. We also mention other diagrammatic approaches employed in the literature.

The MACE methodology consists of three steps (i)–(iii) that are summarized below.

(i) First, starting from the crystal structure, the electronic structure of the material is calculated at the simplified density functional theory (DFT) [20,21] level. This framework uses the LDA or GGA exchange-correlation functionals and a single-determinant wave function. The electronic structure is either left at the LDA(GGA) level [in case the LDA(GGA)+cRPA is employed] or preprocessed to the GW level (if cGW -SIC is employed) supplemented with LRFB (if cGW -SIC+LRFB is employed), as explained in Sec. I.

(ii) The description of the L space is improved by deriving a low-energy effective Hamiltonian (LEH) restricted to the L space. In this LEH, the two-particle part is calculated at the constrained random phase approximation (cRPA) [22,23] at the GGA+cRPA level. At the cGW -SIC and cGW -SIC+LRFB levels, the one-particle part of the LEH is also improved by removing the exchange-correlation double counting term [25] and the self-interaction term [26] (see also Sec. I). This properly describes high-energy (H) states such as core and semicore bands from closed shells, but fails to describe many-body effects and strong electronic correlation in the low-energy (L) subspace near the Fermi level, even with the above preprocessing. In the case of cuprates, this L space is composed of the AB orbital centered on each Cu atom in the CuO_2 plane. The correlation strength is quantified within the ratio u whose value is typically above 7 for the high- T_c cuprates [27,28,30].

(iii) The LEH is solved by a many-body solver, e.g., many-variable Variational Monte Carlo (mVMC) [42]. (See Ref. [43] for a benchmark of the mVMC solver.)

This three-step MACE procedure allows to correctly describe the Mott physics in the mother compound and the SC phase in the carrier doped compound [7,29]. In the mVMC solution, F_{SC} rapidly increases with u in the range $7 \lesssim u \lesssim 8.5$ [7], which suggests an increase in T_c with u [7], in agreement with the positive correlation between u and T_c^{opt} [30] in the same range of values of u . This range corresponds to the weak-coupling and plateau regions [$7 \lesssim u \lesssim 9$ in the u dependence of F_{SC} in Fig. 6(b)]. These results led to the identification of the possibly universal scaling $T_c \simeq 0.16|t_1|F_{\text{SC}}$ in the solution of the AB LEH at the cGW -SIC+LRFB level [7].

To predict the SC character of the material with the above MACE procedure, insights may be obtained even prior to the computationally expensive solution (iii), by examining intermediate quantities within the hierarchical structure of MACE. Notably, the scaling $T_c^{\text{opt}} \simeq 0.16|t_1|F_{\text{SC}}$ proposed in Ref. [7] and the u dependence of F_{SC} in Fig. 6(b) suggest it is possible to anticipate the crystal structure dependence of T_c by studying the crystal structure dependence of LEH parameters (ii), particularly $|t_1|$ and u . Following this idea, we tackle in this paper the derivation of the AB LEH (ii) for Hg1223 as a function of pressure, without performing explicitly the solution (iii), which is left for future studies. Of course, the

explicit many-body solution of the LEH (iii) is necessary to reach the final conclusion.

Furthermore, qualitative insights into the SC may be obtained by deriving the LEH parameters at the simple GGA+cRPA level up to the process (ii), whereas cGW-SIC+LRFB brings a mostly quantitative correction to the LEH parameters [30]. Note that this quantitative correction by cGW-SIC+LRFB is still important to stabilize the SC state with mVMC (iii) in practice: The improvement by cGW-SIC+LRFB increases U and thus u by 10%–15% in Bi2201 and Bi2212 [30], which allows a quantitative estimate of the SC order in the mVMC solution. On the other hand, at the simple GGA+cRPA level, u may be underestimated. Nonetheless, GGA+cRPA still reproduces the dependence of u in the LEH parameters on the materials, and the CPs including pressure effects systematically in accordance with cGW-SIC+LRFB [30], which allows us to extract qualitatively correct trends in the LEH parameters by avoiding the large computational cost [30] of cGW-SIC+LRFB. For instance, in the comparison between Bi2201 ($T_c^{\text{opt}} \simeq 6$ K [2]) and Bi2212 ($T_c^{\text{opt}} \simeq 84$ K [2]), u is larger for Bi2212 at the cGW-SIC+LRFB level, and this qualitative result is also reproduced at the GGA+cRPA level in Ref. [30], Appendix C.

Following the above idea, we mainly employ the GGA+cRPA scheme to derive the AB LEH (ii) for Hg1223. We also employ the cGW-SIC+LRFB scheme in a limited case in Appendix C, as explained in Sec. I.

Besides the MACE approach employed in the present paper and described above, several other approaches allow to take into account diagrams beyond GW , which is necessary to describe the strong electronic correlations in cuprates. These other approaches include the dynamical vertex approximation (D Γ A) [44], the unification of parquet and $GW\Gamma$ methods [45], the quasiparticle self-consistent GW (QSGW) with ladder diagrams [46], as well as the QSGW+DMFT approach employed in Refs. [47,48]. (The QSGW+DMFT approach treats local many-body effects with the quantum impurity solver, but treats nonlocal correlations at the QSGW level.)

The MACE methodology takes into account the strong correlation effect in an alternative fashion without relying on the perturbative diagrammatic expansion of the vertex contribution for the relevant fluctuations. In Ref. [7], both the universal u dependence of F_{SC} and the scaling $T_c^{\text{opt}} \simeq 0.16|t_1|F_{\text{SC}}$ have been obtained using the accurate quantum mVMC solver for the AB band where the dominant many-body quantum fluctuations reside. This quantum many-body solver fully incorporates the effect of temporal and spatial quantum fluctuations on an equal footing. In this approach, the nonlocal interactions are treated at the many-body level in addition to the local interactions.

APPENDIX B: COMPUTATIONAL DETAILS

1. Choice of crystal parameter values

The CP values obtained from neutron diffraction powder and energy-dispersive synchrotron x-ray diffraction experiment [34–36] are summarized in Fig. 2.

There is an uncertainty on the CP values, especially after $P \simeq 9.2$ GPa. Indeed, the experimental P dependence of the

CP values varies between different works. In addition, to our knowledge, the CP values at $P > 9.2$ GPa have not been completely determined in experiment. References [34,35] provide all CP values, but only up to $P \simeq 8.5$ – 9.2 GPa. Reference [36] provides the values of a and c up to $P \simeq 26$ GPa, but not the values of d_j^z . Thus, the CP values are not available within the range $P_{\text{amb}} < P < 45$ GPa that corresponds to the domelike P dependence of T_c^{opt} in Ref. [3].

To verify the robustness of our results with respect to the uncertainty on CP values, we consider CP values obtained by two different theoretical calculations (i and ii), up to 60 GPa. We consider (i) CP values obtained by a structural optimization (denoted as optimized CP values) and (ii) CP values obtained in Zhang *et al.* [33]. We determine first (ii), then (i), as explained below.

On (ii), the values in Zhang *et al.* have been obtained from a theoretical calculation, by means of interatomic potentials. At $P < 9.2$ GPa, these values are in reasonable agreement with the different experimental values from Refs. [34,35]. Although the values of a are overestimated with respect to Refs. [34–36], they are in good agreement with Ref. [36] at 24 GPa.

However, the CP values from Zhang *et al.* are available only up to 20 GPa; thus, we extrapolate their P dependence up to 60 GPa, as follows. We fit the P dependence of a by considering the Murnaghan equation of state

$$\frac{a(P)}{a(P_{\text{amb}})} = \left[1 + \frac{\kappa'}{\kappa} P \right]^{-1/\kappa'}, \quad (\text{B1})$$

as done in Ref. [36]. We deduce the values of the two parameters κ and κ' , which are, respectively, the bulk modulus and its pressure derivative. The same procedure is applied to c , $d_{\text{O(ap)}}^z$, d_{Cu}^z , $d_{\text{Ba,O(o)}}^z = d_{\text{Ba}}^z + d_{\text{buck}}^z$, and $d_{\text{Ca,Ba}}^z = d_{\text{Cu}}^z - d_{\text{Ca}}^z + d_{\text{Ba}}^z$, whose values are extracted from Ref. [33]. In the case of d_{buck}^z , we fit the Cu(o)-O(o)-Cu(o) bond angle as a function of P in Ref. [33], Fig. 5 with Eq. (B1). Then we deduce d_{Ba}^z from $d_{\text{Ba,O(o)}}^z$ and d_{buck}^z , and d_{Ca}^z from $d_{\text{Ca,Ba}}^z$, d_{Cu}^z , and d_{Ba}^z . We checked that values of κ for these CPs from Ref. [33] are reproduced with a difference lower than 0.5%. These values of κ are 1.81×10^{-3} GPa $^{-1}$ for a , 4.61×10^{-3} GPa $^{-1}$ for c , 7.01×10^{-3} GPa $^{-1}$ for $d_{\text{O(ap)}}^z$, 2.94×10^{-3} GPa $^{-1}$ for d_{Cu}^z , 0.64×10^{-3} GPa $^{-1}$ for $d_{\text{Ba-O(o)}}^z$, and 1.535×10^{-3} GPa $^{-1}$ for $d_{\text{Ca-Ba}}^z$. We obtain the CP values in Fig. 2.

On (i), the optimized CP values are obtained by starting from (ii), and performing a structural optimization. We impose the following constraint: The volume $V = a^2c$ of the unit cell remains constant. This allows us to avoid the relaxation of the volume to its value at P_{amb} . Other computational details are the same as those for the self-consistent calculation (see Appendix B 3). Results are shown in Fig. 2.

We deem (i) more reliable than (ii) because the structural optimization allows the rigorous minimization of the free energy of the crystal; thus, we consider (i) in the main analyses of this paper and (ii) as a complement. Still, (ii) is useful to check the robustness of results obtained from (i): We show that both (i) and (ii) yield the same qualitative P dependence of AB LEH parameters (see Sec. V). Of course, it would be

desirable to determine accurately all CP values from P_{amb} to 60 GPa in future experimental works.

Note that, at $P = 60$ GPa, the negative value $d_{\text{buck}}^z \simeq -0.2$ Å obtained for both (i) and (ii) is physical, as discussed below. First, the P dependence of d_{buck}^z at $P > P_{\text{opt}}$ looks robust, because it is similar for (i) and (ii) (see Fig. 2). Second, the negative value of d_{buck}^z has a physical origin: the ‘‘collision’’ between the in-plane O in the OP and the Ca cation. Indeed, when P increases, the distance $d_{\text{Cu}}^z - d_{\text{Ca}}^z$ between the OP and Ca cation is reduced (see Fig. 2). If we see the ions as rigid spheres, the Ca cation ‘‘collides’’ with the in-plane O in the OP, so that the in-plane O is pushed outside of the OP. This explains why d_{buck}^z becomes negative and $|d_{\text{buck}}^z|$ increases. In addition, the rigidity of Cu-O-Cu bonds may play a role in the increase in $|d_{\text{buck}}^z|$: When a is decreased, $|d_{\text{buck}}^z|$ is also increased to prevent the reduction in distance $d_{\text{Cu-O}} = \sqrt{(a/2)^2 + (d_{\text{buck}}^z)^2}$ between Cu and in-plane O.

2. Hole concentration

Next, we take into account the experimental optimal value p_{opt} of the hole concentration p , which realizes T_c^{exp} (the experimental value of T_c) close to $T_c^{\text{opt}} \simeq 138$ K at P_{amb} . Experimentally, hole doping in the CuO_2 planes is realized by introduction of excess oxygen atoms and/or partial substitution of atoms, e.g., Hg by Au, so that the chemical formula of Hg1223 becomes $\text{Hg}_{1-x_s}\text{Au}_{x_s}\text{Ba}_2\text{Ca}_2\text{Cu}_3\text{O}_{8+\delta}$. In that case, a rough estimate of the total hole concentration is $p_{\text{tot}} = 2\delta + x_s$, which corresponds to the average hole concentration per CuO_2 plane $p_{\text{av}} = p_{\text{tot}}/3 = (2\delta + x_s)/3$.

At P_{amb} , previous studies [3,5,37,38] suggest the optimal value of p_{av} is $p_{\text{opt}} \simeq 0.14$ – 0.20 . In Ref. [37], the x_s dependence of T_c^{exp} is explicitly studied: For $\delta = 0.3$, we have $T_c^{\text{exp}} \simeq 133$ K at $x_s = 0$, then T_c^{exp} decreases with x_s , so that the maximum value of $T_c^{\text{exp}} \simeq 133$ K is reached at $p_{\text{av}} = 2\delta/3 \simeq 0.2$. This value of T_c^{exp} corresponds to $T_c^{\text{opt}} \simeq 138$ K [3]. Also, the value $p_{\text{opt}} \simeq 0.2$ is consistent with Ref. [38] in which $T_c^{\text{exp}} \simeq 115$ – 133 K at $p_{\text{av}} \simeq 0.19$ – 0.24 , and also with $p_{\text{opt}} \simeq 0.19$ in Ref. [5]. However, Ref. [3] reports $p_{\text{opt}} \simeq 0.14$ which corresponds to $T_c^{\text{opt}} = 138$ K. Thus, the maximal value of $T_c^{\text{exp}} \simeq 133$ – 138 K is realized for experimental $p_{\text{opt}} \simeq 0.14$ – 0.20 [3,37]. We checked that the LEH parameters are insensitive to the variation in p_{av} in the range $\simeq 0.14$ – 0.20 , as discussed below.

Thus, in our calculations, we realize $p_{\text{av}} = 0.2$ by realizing $p_{\text{tot}} = 0.6$. We do not consider excess oxygen, so that $\delta = 0.0$; instead, we consider $x_s = 0.6$ to compensate the absence of excess oxygen and realize $p_{\text{tot}} = 0.6$.

Also, we checked that our calculations correspond to optimal hole doping $p_{\text{opt}} \simeq 0.14$ – 0.20 not only at P_{amb} but also under pressure, which allows a reliable comparison with the P dependence of T_c^{opt} [3]. According to Ref. [5], p_{opt} is reduced under pressure: We have $p_{\text{opt}} \simeq 0.19$ ($T_c^{\text{opt}} \simeq 134$ K) at P_{amb} but $p_{\text{opt}} \simeq 0.163$ ($T_c^{\text{opt}} \simeq 150$ K) at $P = 12$ GPa. Linear extrapolation of the above pressure dependence of p_{opt} yields $p_{\text{opt}} \simeq 0.12$ at $P_{\text{opt}} = 30$ GPa. However, we have checked that this reduction in p_{opt} does not affect substantially the AB LEH parameters. We consider $x_s = 0.4$ to realize $p_{\text{av}} = 0.133$, and compare with results obtained at $p_{\text{av}} = 0.2$. The values of

TABLE IV. Values of $|t_1^i|$, U^i , and u^i as a function of the average hole concentration per CuO_2 plane p_{av} , at P_{amb} and P_{opt} . We use the optimized CP values.

P	p_{av}	$ t_1^i $	$ t_1^o $	$ t_1^{\text{avg}} $	U^i	U^o	U^{avg}	u^i	u^o	u^{avg}
P_{amb}	0.133	0.526	0.519	0.522	3.97	3.98	3.98	7.55	7.68	7.61
P_{amb}	0.2	0.528	0.523	0.525	3.85	3.79	3.82	7.31	7.26	7.28
P_{opt}	0.133	0.596	0.591	0.594	4.10	3.87	3.99	6.88	6.54	6.71
P_{opt}	0.2	0.598	0.594	0.596	4.13	3.97	4.05	6.91	6.67	6.79

$|t_1^i|$ and u^i at P_{opt} change by only 1%–2% (see Table IV). For completeness, we have also considered $p_{\text{av}} = 0.133$ at P_{amb} : In that case, the values of $|t_1^i|$ change by only 1% and the values of u^i increase by only 3%–6% with respect to $p_{\text{av}} = 0.2$. Thus, the p_{av} dependence of AB LEH parameters is weak, and considering the same value of $p_{\text{av}} = 0.2$ at all pressures is acceptable.

3. DFT calculation

We perform the conventional DFT calculation as follows. We use Quantum ESPRESSO [49,50], and optimized norm-conserving Vanderbilt pseudopotentials (PPs) [51] by employing the GGA-PBE functional [52] together with the pseudopotentials X_ONCV_PBE-1.0.upf ($X = \text{Hg}, \text{Au}, \text{Ba}, \text{Ca}, \text{Cu}, \text{and O}$) [53]. The substitution of Hg by Au is done using the Virtual Crystal Approximation (VCA) [54]. The $\text{Hg}_{1-x_s}\text{Au}_{x_s}$ fictitious atom is abbreviated as ‘‘Hg’’ from now on. We consider nonmagnetic calculations, a plane wave cutoff energy of 100 Ry for wave functions, a Fermi-Dirac smearing of 0.0272 eV, a $12 \times 12 \times 12$ k -point grid for the Brillouin zone sampling in the self-consistent calculation, and a $8 \times 8 \times 3$ k -point grid and 430 bands for the following non-self-consistent calculation.

We obtain the GGA band dispersion in Fig. 3. In this band dispersion, the medium-energy (M) space near the Fermi level is spanned by the 44 $\text{Cu}3d$, $\text{O}2p$, and $\text{Hg}5d$ -like bands from -10 eV to $+3$ eV by defining the origin at the Fermi level.

First, we separate the M space from other bands as follows. We compute the 44 atomiclike Wannier orbitals (ALWOs) spanning the M space (denoted as M-ALWOs), as maximally localized Wannier orbitals [55,56], using the RESPACK code [30,39]. The initial guesses are d , p , and d atomic orbitals centered, respectively at $\text{Cu}(l)$, $\text{O}(l)$ (with $l = i, o$ representing the inner and outer planes, respectively) and at Hg atoms. 44 ALWOs are constructed from the GGA band number from no. 41 to no. 87, which are numbered from the energy bottom of the GGA cutoff. We preserve the band dispersion in the GGA using the inner energy window from the bottom of the lowest band in the M space [the band in black between -7 eV and -10 eV in Figs. 3(a)–3(l)] to the bottom of the lowest empty band outside the M space [the dashed band in black between the Fermi level and $+2$ eV in Figs. 3(a)–3(l)]. Then, the three bands above the 44 M bands are disentangled [57] from the latter.

We obtain the M-ALWOs. They are denoted as $(lj\mathbf{R})$, where \mathbf{R} is the coordinate of the unit cell in the space $[xyz]$ expanded in the $(\mathbf{a}, \mathbf{b}, \mathbf{c})$ frame in Fig. 2, j is the orbital index

and l is the index (defined in Table I) giving the atom located in the cell at \mathbf{R} , on which $(lj\mathbf{R})$ is centered. We then express the GGA one-particle part $h(r)$ in the M-ALWO basis, as

$$h_{j,j'}^{l,l'}(\mathbf{R}) = \int_{\Omega} dr w_{lj\mathbf{0}}^*(r) h(r) w_{l'j'\mathbf{R}}(r), \quad (\text{B2})$$

in which $w_{lj\mathbf{R}}$ is the one-particle wave function of $(lj\mathbf{R})$. From Eq. (B2), we deduce the onsite energy $\epsilon_j^l = h_{j,j}^{l,l}(\mathbf{0})$ of the M-ALWO (lj) at any \mathbf{R} , and the hopping $t_{j,j'}^{l,l'}(\mathbf{R}) = h_{j,j'}^{l,l'}(\mathbf{R})$ between the M-ALWO ($lj\mathbf{0}$) and the M-ALWO ($l'j'\mathbf{R}$). In this paper, we discuss in particular the $\text{Cu}3d_{x^2-y^2}$ and in-plane $\text{O}2p_{\sigma}$ onsite energies and the $\text{Cu}3d_{x^2-y^2}/\text{O}2p_{\sigma}$ hopping in the unit cell $t_{xp}^l = t_{x^2-y^2,p_{\sigma}}^{\text{Cu}(l),\text{O}(l)}$. These quantities are given in Figs. 3(o)–3(q).

$$[\chi_{\text{H}}]_{GG'}(q) = -\frac{4}{N_k} \sum_k \sum_{n_u}^{\text{empty}} \sum_{n_o}^{\text{occupied}} (1 - T_{n_o k} T_{n_u k+q}) \frac{M_{n_o, n_u}^G(k+q, k) [M_{n_o, n_u}^{G'}(k+q, k)]^*}{\Delta_{n_o, n_u}(k, q) - i\eta}, \quad (\text{B3})$$

in which q is a wave vector in the Brillouin zone, G, G' are reciprocal lattice vectors, nk is the Kohn-Sham one-particle state with energy ϵ_{nk} and wave function ψ_{nk} , and $T_{nk} = 1$ if nk belongs to the L space, and $T_{nk} = 0$ else. The charge transfer energy

$$\Delta_{n_o, n_u}(k, q) = \epsilon_{n_u k+q} - \epsilon_{n_o k} \quad (\text{B4})$$

encodes the difference in onsite energies of $n_u k + q$ and $n_o k$, and the interstate matrix element

$$M_{n_o, n_u}^G(k+q, k) = \int_{\Omega} dr \psi_{n_u k+q}^*(r) e^{i(q+G)r} \psi_{n_o k}(r) \quad (\text{B5})$$

encodes the wave functions ψ_{nk} , and also encodes the overlap between ALWOs since the latter are constructed from ψ_{nk} . We deduce the cRPA effective interaction as

$$W_{\text{H}} = (1 - v\chi_{\text{H}})^{-1}v, \quad (\text{B6})$$

in which v is the bare Coulomb interaction. We deduce the onsite Coulomb repulsion in Eq. (9).

APPENDIX C: CORRECTION OF u AND $|t_1|$: IMPROVEMENT FROM THE GGA+CRPA LEVEL TO THE cGW-SIC+LRFB LEVEL

Here we give details on the calculation of x_{LRFB} and y_{LRFB} in Eqs. (2) and (3) which allows us to deduce $u_{\text{cGW-SIC+LRFB}}$ and $|t_1|_{\text{cGW-SIC+LRFB}}$ in Hg1223. [This corresponds to the correction (C) mentioned in Sec. II.]

First, we address again the computational load of the direct cGW-SIC+LRFB calculation for Hg1223. This calculation requires the LRFB preprocessing, whose extension to the cuprates with $N_{\ell} = 3$ is computationally demanding, because one needs to solve the three-orbital Hamiltonian consisting of three CuO_2 planes in total by an accurate quantum many-body solver (see Ref. [30] for details) by taking into account the inter- CuO_2 plane hopping and interaction parameters. We leave such an extension for future studies. Instead, we employ

4. Low-energy subspace

Then we focus on the L space, which is spanned by the $\text{Cu}3d_{x^2-y^2}/\text{O}2p_{\sigma}$ AB band shown in red in Figs. 3(a)–3(g). To construct the AB maximally localized Wannier orbitals, the initial guesses are the $d_{x^2-y^2}$ atomic orbitals centered on each of the three Cu(l) atoms in the unit cell. The band window is essentially the M space, but we exclude the $N_{\text{excl}} = 14$ lowest bands from it to avoid catching the B/NB $\text{Cu}3d_{x^2-y^2}/\text{O}2p_{\sigma}$ character. Then, in the band window, we disentangle the 29 other bands from the AB band.

5. Constrained polarization and effective interaction

Then we compute the cRPA polarization at zero frequency. It is expressed as [39]

the procedure (C1) and (C2) mentioned in Sec. II, because it already allows us to reach physically transparent understanding.

In the procedure (C1), we improve the AB LEH from the GGA+cRPA level to the cGW-SIC level. Since the ratios $u_{\text{cGW-SIC}}/u^{\text{avg}}$ and $|t_1|_{\text{cGW-SIC}}/|t_1^{\text{avg}}|$ may have strong materials dependence and also pressure dependence, due to the diversity of the global band structure outside of the AB band, we need to perform this procedure with respect to each material and pressure separately. For instance, in Hg1223, we have $u_{\text{cGW-SIC}}/u^{\text{avg}} \simeq 1.36$ at P_{amb} and $\simeq 1.21$ at 30 GPa. The calculated cGW-SIC level of the parameters is shown in Table V; computational details of the cGW-SIC calculation are given at the end of this Appendix.

To perform (C2), we employ the material independent constants x_{LRFB} and y_{LRFB} to correct the cGW-SIC results obtained in (C1), because this procedure is only to readjust mainly the onsite Coulomb interaction U and this correction is materials insensitive. This readjustment arises from the correction of the relative chemical potential between the AB and B/NB bands to keep the electron fillings of the $\text{Cu}3d$ and $\text{O}2p$ orbitals, while the band structure of AB and B/NB bands by readjusting their chemical potentials and this chemical potential shift are indeed material insensitive in the known four compounds [30] because of the similar AB and B/NB band structures of the cuprates in general. In fact, our explicit calculations of x_{LRFB} and y_{LRFB} for several other cuprates (Hg1201, CaCuO_2 , Bi2201, and Bi2212) show that, near optimal hole doping, $x_{\text{LRFB}} \simeq 0.91$ – 0.97 and $y_{\text{LRFB}} \simeq 0.99$ – 1.06 are rather universal and almost independent of the material. Thus, it may be reasonable to assume that Hg1223 near the optimal hole doping has similar values of x_{LRFB} or y_{LRFB} , and the narrow range of uncertainty allows accurate estimation of the Hamiltonian parameters.

Still, the small uncertainty on $x_{\text{LRFB}} \simeq 0.91$ – 0.97 causes a possible quantitative error on the P dependence of $T_{\text{c}}^{\text{est}}$ [see Fig. 1(b)], even though the qualitative dome structure is robust. We thus narrow the estimate of x_{LRFB} as follows. In

TABLE V. Values of u and $|t_1|$ calculated for Hg1201, CaCuO₂, Bi2201, Bi2212, and Hg1223, at the average hole concentration per CuO₂ plane p_{av} close to the optimal hole concentration. N_ℓ is the number of adjacent CuO₂ layers sandwiched between block layers. On Hg1201, CaCuO₂, Bi2201, and Bi2212, we show the values of $u_{cGW-SIC+LRFB}$ and $|t_1|_{cGW-SIC+LRFB}$ at P_{amb} taken from Ref. [30], and the values of $u_{cGW-SIC}$ and $|t_1|_{cGW-SIC}$ at P_{amb} calculated in this paper. The values of x_{LRFB} and y_{LRFB} at P_{amb} are calculated from Eqs. (2) and (3). On Hg1223, we show the values of u^{avg} and $|t_1^{avg}|$ at the GGA+cRPA level, and the values of $u_{cGW-SIC}$ and $|t_1|_{cGW-SIC}$ calculated in this paper at P_{amb} , 30 GPa and 60 GPa. We also show the values of $u_{cGW-SIC+LRFB}$ and $|t_1|_{cGW-SIC+LRFB}$ estimated from Eqs. (2) and (3) with the choices of $x_{LRFB} = 0.91, 0.95, \text{ and } 0.97$ and $y_{LRFB} = 1.0$ inferred by analyzing other compounds (see the main text). We also show the values of $|t_1|_{cGW-SIC+LRFB}$ obtained after applying the correction (D).

	Hg1201	CaCuO ₂	Bi2201	Bi2212	Hg1223	Hg1223	Hg1223
P (GPa)	0	0	0	0	0	30	60
p_{av}	0.1	0.1	0.2	0.2	0.2	0.2	0.2
N_ℓ	1	∞	1	2	3	3	3
$1/N_\ell$	1	0	1	0.5	0.333	0.333	0.333
u^{avg}	—	—	—	—	7.22	6.80	6.35
$u_{cGW-SIC}$	8.06	8.39	9.06	9.97	9.83	8.21	7.23
$u_{cGW-SIC+LRFB}$	7.35	8.10	8.34	9.37	—	—	—
x_{LRFB}	0.91	0.97	0.92	0.94	—	—	—
Estimated x_{LRFB}	—	—	—	—	0.91/0.95/0.97	0.91/0.95/0.97	0.91/0.95/0.97
$u_{cGW-SIC+LRFB}$	—	—	—	—	8.95/9.34/9.54	7.47/7.80/7.96	6.58/6.87/7.01
$ t_1^{avg} $	—	—	—	—	0.528	0.596	0.643
$ t_1 _{cGW-SIC}$	0.526	0.526	0.498	0.436	0.485	0.569	0.615
$ t_1 _{cGW-SIC+LRFB}$	0.544	0.521	0.527	0.451	—	—	—
y_{LRFB}	1.034	0.990	1.058	1.034	—	—	—
Estimated y_{LRFB}	—	—	—	—	1.0	1.0	1.0
$ t_1 _{cGW-SIC+LRFB}$	—	—	—	—	0.485	0.569	0.615
$ t_1 _{cGW-SIC+LRFB}$ [after (D)]	—	—	—	—	0.485	0.593	0.642

Fig. 7 we see a small but systematic linear dependence of x_{LRFB} on $1/N_\ell$. Linear interpolation of the $1/N_\ell$ dependence of x_{LRFB} yields $x_{LRFB}^{est} = 0.951 \simeq 0.95$ at $N_\ell = 3$. Thus, we assume $x_{LRFB} = 0.95$ in Hg1223; for completeness, we also admit the range of uncertainty $x_{LRFB} \simeq 0.91\text{--}0.97$. On y_{LRFB} , there is no clear $1/N_\ell$ dependence of y_{LRFB} , so that we simply assume $y_{LRFB} = 1.0$. (Note that the results shown in Fig. 1 and Fig. 6 do not depend on the value of y_{LRFB} .) We deduce the values of $u_{cGW-SIC+LRFB}$ and $|t_1|_{cGW-SIC+LRFB}$ that are shown in Table V.

The universality of calculated x_{LRFB} and y_{LRFB} may be understood as follows. The LRFB corrects the value of ΔE_{xp}

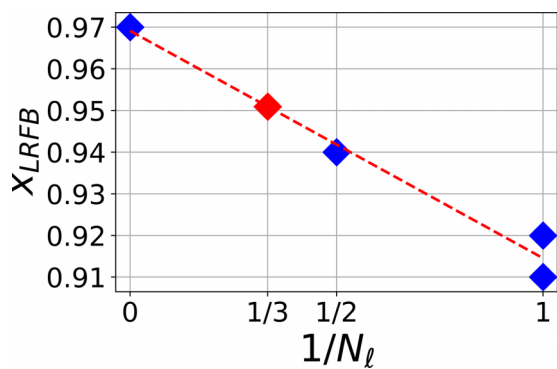


FIG. 7. $1/N_\ell$ dependence of calculated x_{LRFB} (blue symbols) for Hg1201, CaCuO₂, Bi2201, and Bi2212 listed in Table V and their linear fitting (red dashed line). Red diamond is the estimate for Hg1223 ($x_{LRFB}^{est} = 0.951$) obtained from the interpolation at $1/N_\ell = 1/3$.

by an amount $\Delta\mu$ whose value is similar for all optimally doped compounds (we obtain $\Delta\mu \simeq 1.1\text{--}1.4$ eV in Ref. [30], Table IV). This universality in $\Delta\mu$ is consistent with the universality in x_{LRFB} and y_{LRFB} .

Note that $u_{cGW-SIC+LRFB}$ and $|t_1|_{cGW-SIC+LRFB}$ are rough estimates of the actual cGW-SIC+LRFB result. In the actual cGW-SIC+LRFB calculation, more complex factors such as the self-doping of the IP and OP [38] and the Coulomb interaction between the IP and OP may affect the result of the LRFB calculation. (Clarification of these factors is left for future studies.) Nonetheless, the simple above estimate supports the assumption (B) in Sec. I.

Computational details of the cGW-SIC scheme. We apply the cGW-SIC scheme to Hg1201, Bi2201, Bi2212, CaCuO₂, and Hg1223 as follows. On Hg1201, Bi2201, Bi2212, and CaCuO₂, we consider the same computational conditions and hole concentration as in Ref. [30]. On Hg1223, we first preprocess the 44 bands within the M space from the GGA level to the GW level. (The GW preprocessing is presented in detail in Ref. [30], Appendix A2.) The random phase approximation (RPA) polarization is calculated using 100 real frequencies and 30 imaginary frequencies; the maximum modulus of the frequency is 19.8 Ha. The exchange-correlation potential is sampled in the real space using a $120 \times 120 \times 540$ grid to sample the unit cell. In the calculation of the GW self-energy, we reduce the computational cost by employing the scheme sketched in Ref. [30], Appendix E, with the cutoff energy $\epsilon = 0.01$ eV. Other computational details are the same as those in Appendix B. We obtain the GW electronic structure, in which the M bands are preprocessed at the GW level and the other bands are left at the GGA level. Then, we derive the AB

LEH. We start from the *GW* electronic structure and construct the AB MLWO. The band window is the M space but we exclude the N_{excl} lowest bands from it. (We use $N_{\text{excl}} = 9$ at P_{amb} , and $N_{\text{excl}} = 10$ at 30 GPa and 60 GPa.) Then we use the cRPA to calculate the two-particle part and U . We also use the c*GW* to calculate the one-particle part and $|t_1|$. (Details about the c*GW* scheme can be found in Ref. [30], Appendix A5.)

APPENDIX D: CORRECTION OF $|t_1|$ BY CORRECTING THE CELL PARAMETER a

Here we give details about the correction (D) mentioned in Sec. I. To correct the P dependence of $|t_1|$, we correct (i) the P dependence of a in Fig. 2, then combine the corrected (i) with (ii) the a dependence of $|t_1|$ estimated in Appendix E2, Eq. (E1).

On (i), the P dependence of a is shown in Fig. 2. The experimental values of a are available at P_{amb} [34] and $P = 8.5$ GPa, but not at $P > 8.5$ GPa. At P_{amb} , the experimental a and optimized a are in very good agreement (the difference is $\simeq 0.004$ Å). However, at $P = 8.5$ GPa, the optimized a overestimates the experimental a by $\simeq 0.05$ Å. We assume that such an overestimation also happens at $P > 8.5$ GPa, and we correct the P dependence of optimized a accordingly. The values of the P -dependent correction $\Delta a(P)$ are $\Delta a(P) = 0$ Å if $P = P_{\text{amb}}$ and $\Delta a(P) = \Delta a = -0.05$ Å if $P > P_{\text{amb}}$, and the P -dependent corrected a is denoted as

$$\tilde{a}(P) = a(P) + \Delta a(P). \quad (\text{D1})$$

On (ii), Eq. (E1) gives $|t_1|(a) \propto 1/a^3$. Combination with Eq. (D1) yields

$$|t_1|[\tilde{a}(P)] = \frac{|t_1|[a(P)]}{1 + 3 \frac{\Delta a(P)}{a(P)} + 3 \left[\frac{\Delta a(P)}{a(P)} \right]^2 + \left[\frac{\Delta a(P)}{a(P)} \right]^3}, \quad (\text{D2})$$

which allows us to determine $|t_1|[\tilde{a}(P)]$ as a function of $|t_1|[a(P)]$. The last two terms in the denominator of Eq. (D2) are negligible because $|\Delta a(P)/a(P)| \simeq 0.014 \ll 1$, so that we have

$$|t_1|[\tilde{a}(P)] = \frac{|t_1|[a(P)]}{1 + 3 \frac{\Delta a(P)}{a(P)}}. \quad (\text{D3})$$

[Note that $|t_1|[\tilde{a}(P)] \geq |t_1|[a(P)]$ because $\Delta a(P) \leq 0$.] We use Eq. (D3) to correct the P dependence of $|t_1|_{\text{cGW-SIC+“LRFB”}}$. The values of $|t_1|_{\text{cGW-SIC+“LRFB”}}$ that are obtained after applying (D) are shown in Table V at P_{amb} , 30 GPa and 60 GPa.

For completeness, we mention a limitation of the correction (D): It relies on the dependencies (i) and (ii) mentioned above, and (ii) is determined at the GGA+cRPA level. The only way to improve slightly the approximation in (D) and Eq. (D3) would be to take the optimized CPs at $P = 30$ GPa and reduce the cell parameter a by 0.05 Å (the estimated difference between optimized a and experimental a), then perform explicitly the c*GW*-SIC calculation from the CP with the reduced a , then deduce $|t_1|_{\text{cGW-SIC+“LRFB”}}$ and $u_{\text{cGW-SIC+“LRFB”}}$. However, this improvement is computationally expensive, and we do not expect it to change the results significantly. Thus, we do not consider it here.

APPENDIX E: PRESSURE DEPENDENCE OF INTERMEDIATE QUANTITIES

1. Pressure dependence of the DFT band structure and Madelung potential

Here, as a complement to Sec. IV, we show that [MW] is robust with respect to the definition of uniaxial pressure and with respect to the uncertainty on CP values. First, [MW] is caused by P_a^{buck} rather than P_c^{buck} (see Fig. 8), which is consistent with Fig. 3 in which [MW] is caused by P_a rather than P_c : The main origin of [MW] is indeed the reduction in a , and the variation in d_{buck}^z with P_a^{buck} does not affect this result. Also, if we use the CP values from Zhang *et al.* instead of the optimized CP values, [MW] is well reproduced (see Fig. 9).

In addition, we discuss the mechanisms of [Mε] and [MW] in terms of Madelung potential created by ions in the crystal. As shown in Sec. IV, [Mε] and [MW] are mainly caused by the reduction in a . This may be understood as follows. The main contribution of the Madelung potential felt by electrons in the CuO₂ plane is from the positive Cu and negative O ion within the plane. Then the energy of an electron at the Cu3*d* orbital gets higher when the surrounding O ions become closer to the Cu site, namely, if a is reduced. On the contrary, an electron at the O2*p_σ* orbital feels opposite for the reduced a . This makes the difference of the electronic levels for the Cu3*d_{x²-y²}* and O2*p_σ* larger. More precise calculation including long-range Coulomb potential by DFT supports this simple view is essentially correct.

The P_a induced increase in energy of Cu3*d* bands is illustrated in Figs. 10(a), 10(b), and 10(c). The application of P_a increases the absolute energy of Cu3*d* bands. (The absolute energy is defined as the energy without renormalization with respect to the Fermi level.) Note that examining the pressure dependence of absolute energies does make sense, because the chemical composition of the crystal is not modified by the application of pressure.

The application of P_c increases the energy of not only Cu3*d* bands but also O2*p* bands in Figs. 10(a), 10(d), and 10(e), so that [MW] does not occur. This can also be understood in terms of Madelung potential from in-plane O anions. When P_c is applied, the distance d_{Cu}^z between the IP and OP is reduced. This reduces not only (i) the interatomic distance between the O anion in the OP (IP) and the Cu in the IP (OP), but also (ii) the interatomic distance between the O anion in the OP (IP) and the O in the IP (OP). The concomitant reduction in (i) and (ii) causes the concomitant increase in Cu3*d* and O2*p* electronic levels.

2. Pressure dependence of the onsite bare interaction and Cu3*d_{x²-y²}*/O2*p_σ* charge transfer energy

Here, as a complement to Sec. VB, we discuss the following points:

(a) The increase in onsite bare interaction v is caused by the reduction in Cu3*d_{x²-y²}*/O2*p_σ* hybridization when ΔE_{xp} increases.

(b) The concomitant increases in $|t_1|$ and v when a decreases can be understood by further analysis of the a dependence of quantities.

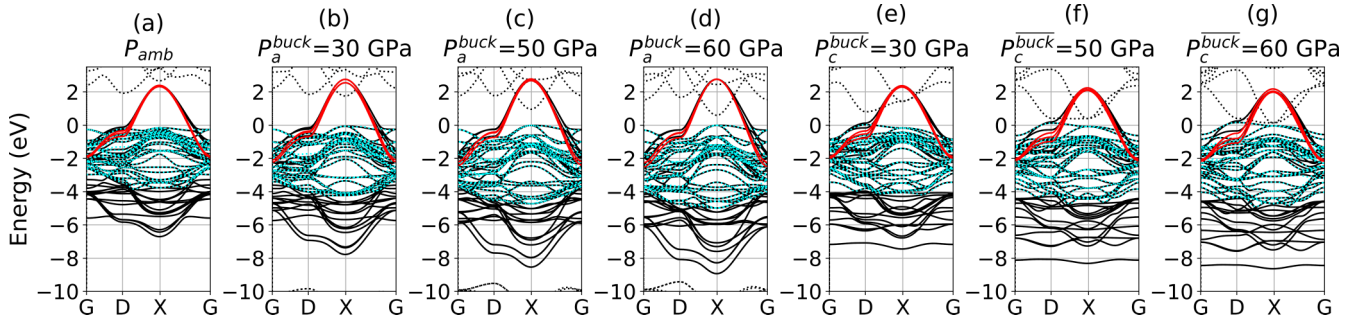


FIG. 8. P_a^{buck} and P_c^{buck} dependence of the GGA band structure obtained using the optimized CP values. Notations are the same as those in Fig. 3.

(c) The reduction in the correlation between v^l and ΔE_{xp}^l at $P > P_{\text{opt}}$ originates from the nonequivalence of the IP and OP, especially the buckling of Cu-O-Cu bonds in the OP. }

On (a), a first remark is that the $\text{Cu}3d_{x^2-y^2}/\text{O}2p_\sigma$ hybridization reduces v by reducing the atomic $\text{Cu}3d_{x^2-y^2}$ character of the AB orbital. In the AB orbital, the onsite bare interaction is $v_x^{\text{avg}} \simeq 14.5\text{--}15.5$ eV, but in the $\text{Cu}3d_{x^2-y^2}$ M-ALWO, the onsite bare interaction $v_x^{\text{avg}} \simeq 25.5$ eV is larger [see Fig. 11(a)]. This is because the $\text{Cu}3d_{x^2-y^2}$ M-ALWO has atomic character and is more localized than the AB orbital. In the limit of zero hybridization, the AB orbital is equivalent to the $\text{Cu}3d_{x^2-y^2}$ M-ALWO if we neglect the effect of other orbitals: In that case, $v_x^{\text{avg}} = v_x^{\text{avg}}$. However, the hybridization is always nonzero in the realistic cuprate, so that the atomic $\text{Cu}3d_{x^2-y^2}$ character of the AB orbital is reduced.

Second, the importance of the $\text{Cu}3d_{x^2-y^2}/\text{O}2p_\sigma$ hybridization decreases with P . The importance of the hybridization is roughly encoded in the ratio $O_{xp} = |t_{xp}|/\Delta E_{xp}$ between the $\text{Cu}3d_{x^2-y^2}/\text{O}2p_\sigma$ hopping amplitude and $\text{Cu}3d_{x^2-y^2}/\text{O}2p_\sigma$ charge transfer energy. O_{xp} decreases when the hybridization is reduced and becomes zero when the hybridization is negligible. And O_{xp}^{avg} decreases with P [see Fig. 11(b)].

Thus, the atomic $\text{Cu}3d_{x^2-y^2}$ character of the AB orbital increases with P : We interpret this as the origin of the increase in v . To confirm this, we show explicitly that $v_x^{\text{avg}} \simeq v_x^{\text{avg}}$ in the limit of zero hybridization. Let us consider the O_{xp}^{avg} dependence of v_x^{avg} in Fig. 11(c), which is obtained by combining the P dependencies of v_x^{avg} and O_{xp}^{avg} in Figs. 11(a) and 11(b). In the *ab initio* calculation, we have $O_{xp}^{\text{avg}} \simeq 0.7\text{--}0.8$, so that the O_{xp} dependence of v_x^{avg} can be explicitly obtained only within this range. However, the value of v_x^{avg} in the limit of zero hybridization may be estimated by performing a linear

extrapolation of the *ab initio* O_{xp}^{avg} dependence of v_x^{avg} . The extrapolation yields $v_x^{\text{avg}} \simeq 24$ eV at $O_{xp}^{\text{avg}} = 0$ [see Fig. 11(c)], which is similar to $v_x^{\text{avg}} \simeq 25.5$ eV. This suggests the AB orbital becomes the $\text{Cu}3d_{x^2-y^2}$ M-ALWO in the limit of zero hybridization, as mentioned above.

On (b), we analyze the a dependence of $|t_1^{\text{avg}}|$, $\Delta E_{xp}^{\text{avg}}$ and $|t_{xp}^{\text{avg}}|$, as well as the average values O_{xp}^{avg} and T_{xp}^{avg} of $O_{xp}^l = |t_{xp}^l|/\Delta E_{xp}^l$ and $T_{xp}^l = |t_{xp}^l|^2/\Delta E_{xp}^l$: the key point is that, when a decreases, O_{xp}^{avg} decreases whereas $|t_1^{\text{avg}}| \propto T_{xp}^{\text{avg}}$ increases. To obtain the a dependence of the above quantities, we take the values of a as a function of pressure in Fig. 2 and combine them with the P_a dependence of $|t_1^l|$, ΔE_{xp}^l and $|t_{xp}^l|$ in Figs. 5(a), 5(f), and 5(g). Note that we consider the P_a dependence instead of the P dependence. This is because the application of P_a modifies only the value of a : This allows to extract accurately the a dependence while avoiding the d_i^z dependence of quantities.

We interpolate the a dependencies of the above quantities, using the fitting function $f(a) = Ca^\beta$, where β and C are the fitting parameters. We examine the values of β , which encode the speed of variation in quantities with a . The obtained values of β are shown in Fig. 12.

First, we have

$$|t_1^{\text{avg}}| \propto T_{xp}^{\text{avg}} \propto 1/a^3. \quad (\text{E1})$$

Indeed, the value of β for $|t_1^{\text{avg}}|$ is $\beta(|t_1^{\text{avg}}|) \simeq -2.88$, which is very close to -3 . This is consistent with the $1/r^3$ decay of the density-density correlation function [58]. Also, $\beta(T_{xp}^{\text{avg}}) \simeq -2.89$ is almost identical to $\beta(|t_1^{\text{avg}}|)$.

Second, we have

$$O_{xp}^{\text{avg}} \propto a. \quad (\text{E2})$$

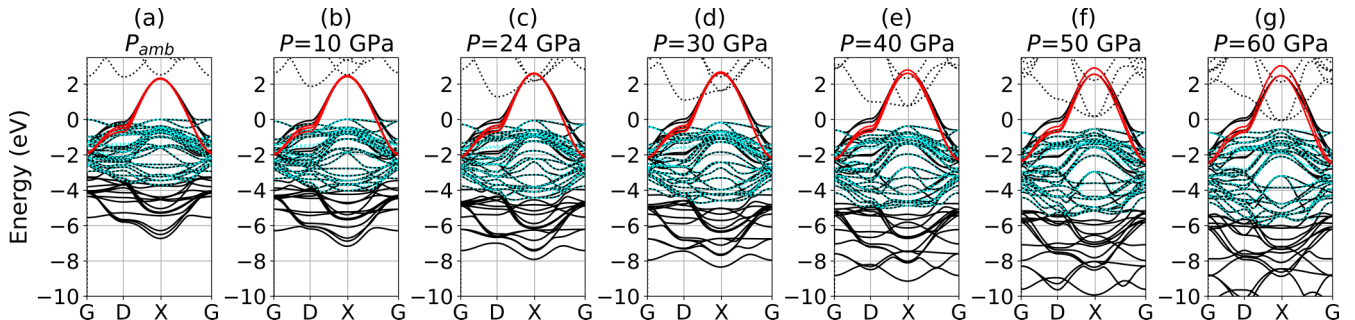


FIG. 9. P dependence of the GGA band structure obtained using the CP values from Zhang *et al.* Notations are the same as those in Fig. 3.

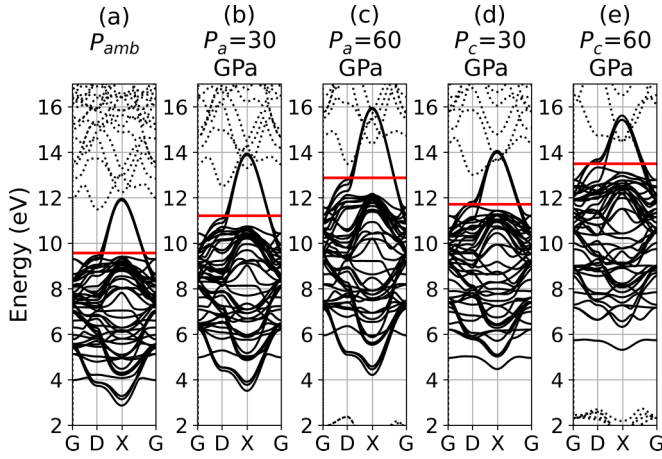


FIG. 10. P_a and P_c dependencies of the band structure and Fermi energy. We show the bands inside the M space (solid black color) and outside M space (dotted black color). These band structures correspond to those in Figs. 3(h), 3(i), 3(k), 3(l), and 3(n), except that the band energies are not renormalized with respect to the Fermi energy. The latter is given by the horizontal line in red color.

Indeed, the O_{xp}^{avg} dependence of a is almost linear: $\beta(O_{xp}^{\text{avg}}) = 0.98$ is very close to 1.

The above equations (E1) and (E2) show that both $|t_1^i|$ and v^i increase when a decreases. Indeed, in item (a), we have clarified that v^{avg} increases when O_{xp}^{avg} decreases, and Eq. (E2) shows that O_{xp}^{avg} decreases when a decreases. Note that $\beta(\Delta E_{xp}^{\text{avg}}) < \beta(|t_{xp}^{\text{avg}}|) < 0$: This is the origin of the positive value of $\beta(O_{xp}^{\text{avg}})$. On the other hand, $2\beta(|t_{xp}^{\text{avg}}|) < \beta(\Delta E_{xp}^{\text{avg}}) < 0$: This is the origin of the negative value of $\beta(|t_1^{\text{avg}}|) \simeq \beta(T_{xp}^{\text{avg}})$.

On (c), the nonequivalence of the IP and OP causes a slight difference in the ΔE_{xp}^l dependence of v^l for $l = i$ and $l = o$ [see Figs. 4(e), 4(f), 4(l), and 4(m) at $P > P_{\text{opt}}$]. This is simply because $|t_{xp}^o|$ is reduced at $P > P_{\text{opt}}$ due to the

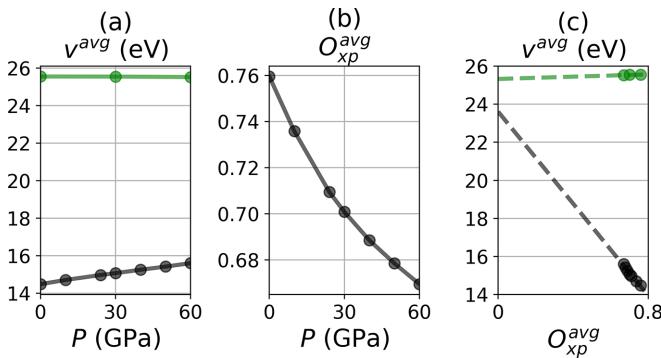


FIG. 11. (a) P dependence of the average value v^{avg} over the IP and OP of the onsite bare interaction. We show v^{avg} in the AB (black dots) and $\text{Cu}3d_{x^2-y^2}$ (green dots) Wannier orbitals. (b) P dependence of the average value O_{xp}^{avg} of the ratio $O_{xp}^l = |t_{xp}^l|/\Delta E_{xp}^l$, which encodes the $\text{Cu}3d_{x^2-y^2}/O2p_\sigma$ hybridization. (c) O_{xp}^{avg} dependence of v^{avg} in the AB (black dots) and $\text{Cu}3d_{x^2-y^2}$ (green dots) Wannier orbitals. The dashed lines show the linear extrapolation to $O_{xp}^{\text{avg}} = 0$ (the limit in which the $\text{Cu}3d_{x^2-y^2}/O2p_\sigma$ hybridization becomes negligible).

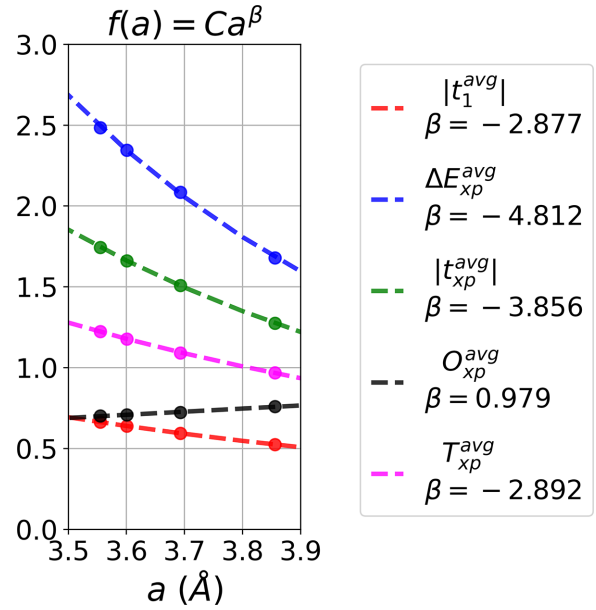


FIG. 12. Cell parameter a dependence of $|t_1^{\text{avg}}|$, $\Delta E_{xp}^{\text{avg}}$, $|t_{xp}^{\text{avg}}|$, and the average values O_{xp}^{avg} and T_{xp}^{avg} of $O_{xp}^l = |t_{xp}^l|/\Delta E_{xp}^l$ and $T_{xp}^l = |t_{xp}^l|^2/\Delta E_{xp}^l$ (dots). We start from the optimized CP values at P_{amb} and apply P_a to modify only the value of a . The dashed curves show the interpolation of the a dependence by the function $f(a) = Ca^\beta$, where β and C are the fitting parameters. The legend shows the obtained values of β .

increase in $|d_{\text{buck}}^z|$ [see Fig. 4(g)]. This contributes to reduce $O_{xp}^o = |t_{xp}^o|/\Delta E_{xp}^o$, which increases v^o [see item (a)]. This explains why, at $P > P_{\text{opt}}$, $v^o \simeq v^i$ even though $\Delta E_{xp}^o < \Delta E_{xp}^i$ [see Figs. 4(e) and 4(f)]. On the other hand, if we apply only P_a (which modifies only a without modifying d_{buck}^z), $|t_{xp}^o|$ is not reduced with respect to $|t_{xp}^i|$ [see Fig. 4(g)], and the ΔE_{xp}^l dependence of v^l is very similar for $l = i$ and $l = o$ [see Figs. 4(e) and 4(f)].

The nonequivalence of the IP and OP also causes a slight difference in the P dependence of ΔE_{xp}^l for $l = i$ and $l = o$ in Figs. 4(f) and 4(m). This is because ΔE_{xp}^l depends not only on a , but also on d_{Ca}^z [see Fig. 13(f) in Appendix F]. For instance, ΔE_{xp}^i (ΔE_{xp}^o) increases (decreases) when d_{Ca}^z decreases. And, $d_{\text{Ca}}^z \simeq 1.48 \text{ \AA}$ in the optimized CP values is smaller than $d_{\text{Ca}}^z \simeq 1.59 \text{ \AA}$ in the CP values from Zhang *et al.* This is why $\Delta E_{xp}^i > \Delta E_{xp}^o$ for the optimized CP values, but $\Delta E_{xp}^i < \Delta E_{xp}^o$ for the values from Zhang *et al.* [see Figs. 4(f) and 4(m)].

3. Pressure dependence of the screening

Here, as a complement to Sec. V C, we discuss the uniaxial pressure dependence of R^{avg} , from which the dome structure in the uniform pressure dependence of R^{avg} originates. } First, we discuss the P_a dependence of R^{avg} in Fig. 5(d).

(i) At $P_a < P_{\text{opt}}$, the increase in R^{avg} is explained by the broadening [MW] of the GGA band dispersion. More precisely, the origin is the increase in charge transfer energies (B4) (schematically denoted as Δ in this Appendix) between occupied and empty bands, due to [MW] discussed in Sec. IV. The increase in Δ participates in the decrease of the amplitude

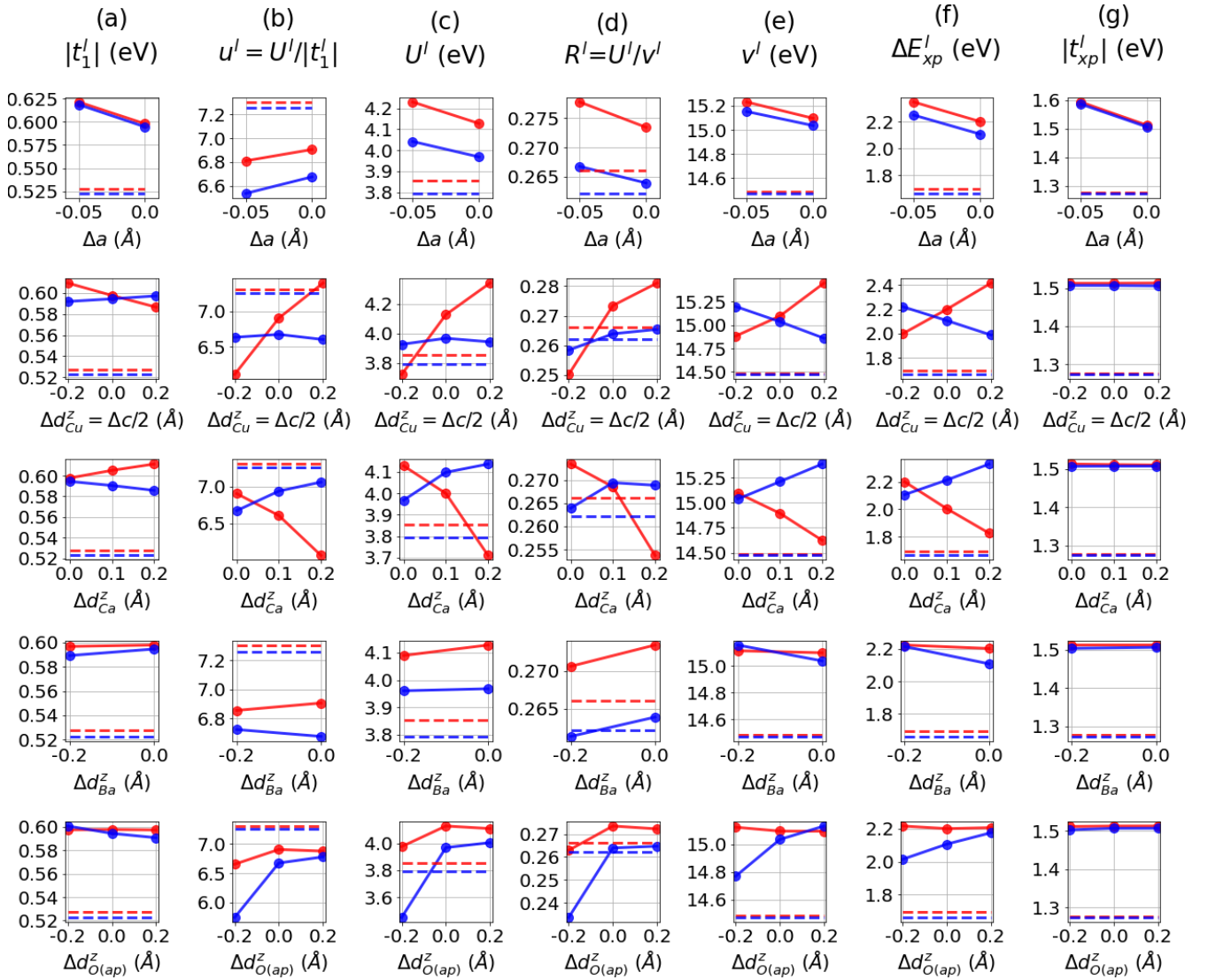


FIG. 13. CP dependencies of $|t_1^l|$, u^l , U^l , $R^l = U^l/v^l$, v^l , ΔE_{xp}^l and $|t_{xp}^l|$. We show quantities in the IP ($l = i$) and OP ($l = o$) in red and blue, respectively. The quantities are obtained using the optimized CP values at $P_{\text{opt}} = 30$ GPa, and modifying the values of a , c , and d_i^z by Δa , Δc , and Δd_i^z , respectively. Note that when Δd_{Cu}^z is applied, $\Delta c = 2\Delta d_{\text{Cu}}^z$ is also applied so that all interatomic distances in the block layer remain unchanged. The horizontal dashed lines represent the values at P_{amb} for comparison.

of the cRPA polarization (B3), schematically denoted as $|\chi| \propto 1/\Delta$. This reduces the cRPA screening and thus increases R^{avg} .

(ii) At $P_a > P_{\text{opt}}$, the increase in R^{avg} ceases. This is because the effect of [MW] is progressively reduced: We have $\partial|\chi|/\partial\Delta \propto -1/\Delta^2$, so that the larger P_a and thus Δ , the smaller the decrease in $|\chi|$ when Δ is further increased, and the less important the effect of [MW]. In addition, when P_a increases, the charge transfer energy $\Delta_{\text{M-empty}}$ between the M bands and empty bands outside M space is reduced, because the energy of the Cu3d bands increases [see Figs. 10(a), 10(b), and 10(c)]. This may contribute to increase $|\chi| \propto 1/\Delta_{\text{M-empty}}$ and cancel the effect of [MW] at high pressure.

Second, we discuss the decrease in the P_c dependence of R^{avg} in Fig. 5(d). This is because [MW] does not occur when P_c is applied, contrary to P_a . Thus, Δ does not increase. On the other hand, $\Delta_{\text{M-empty}}$ is reduced because the energy of Cu3d

bands increases [see Figs. 10(a), 10(d), and 10(e)]. As a result, $|\chi| \propto 1/\Delta_{\text{M-empty}}$ increases.

APPENDIX F: CRYSTAL PARAMETER DEPENDENCE OF EFFECTIVE HAMILTONIAN PARAMETERS AT OPTIMAL PRESSURE

Here, as a complement to Sec. V, we analyze the CP dependencies of AB LEH parameters around P_{opt} . We start from the optimized CP values at P_{opt} and modify separately the values of each CP. The modified values are given in Fig. 2 (open squares). The CP dependencies of AB LEH parameters are shown in Fig. 13.

We summarize the main results below:

- (i) As for $|t_1^l|$, the a dependence is the strongest.
- (ii) As for u^i , the d_{Ca}^z and d_{Cu}^z dependencies are the strongest.

(iii) As for u^o , the d_{Ca}^z and $d_{\text{O(ap)}}^z$ dependencies are the strongest.

Also, (ii) and (iii) suggest the origin of the decrease in R^l at $P > P_{\text{scr}}$ in Sec. V C, Figs. 4(d) and 4(k): The decreases in R^i and R^o are caused, respectively, by the decreases in d_{Cu}^z and $d_{\text{O(ap)}}^z$.

a dependence of AB LEH parameters. At P_{opt} , the optimized value of $a \simeq 3.69 \text{ \AA}$ is the same as that from Zhang *et al.*. Still, this value might be overestimated. Indeed, the P dependence of experimental values [34,35] shows the faster decrease at lower pressures (see Fig. 2). Thus, we consider the modification Δa of a at P_{opt} , such that $-0.05 \text{ \AA} \leq \Delta a \leq 0 \text{ \AA}$ at P_{opt} .

The a dependence of $|t_1|$ is strong [see Fig. 13(a)], as discussed in Sec. V A. We note that the 15% increase in $|t_1|$ from P_{amb} to P_{opt} becomes 18%–19% if $\Delta a = -0.05 \text{ \AA}$. Thus, the 3% difference between the increase in $|t_1|$ and that in T_c^{opt} may be understood by admitting the above uncertainty on a at P_{opt} (see the discussion in Sec. VI).

d_{Ca}^z dependence of AB LEH parameters. The optimized value $d_{\text{Ca}}^z \simeq 1.48 \text{ \AA}$ is lower than that from Zhang *et al.* ($d_{\text{Ca}}^z \simeq 1.59 \text{ \AA}$). Thus, we consider $0.0 \text{ \AA} \leq \Delta d_{\text{Ca}}^z \leq +0.2 \text{ \AA}$ to examine the d_{Ca}^z dependence of AB LEH parameters.

Increasing d_{Ca}^z causes the rapid decrease in u^i and increase in u^o [see Fig. 13(b)], due to the decrease in ΔE_{xp}^i and increase in ΔE_{xp}^o [see Fig. 13(f)]. Indeed, v^l and R^l are correlated with ΔE_{xp}^l . The correlation between v^l and ΔE_{xp}^l has been discussed in Appendix E 2, and the increase in ΔE_{xp}^l also contributes to increase R^l by reducing the cRPA screening between $\text{Cu}3d_{x^2-y^2}/\text{O}2p_\sigma$ B/NB and AB bands.

The increase (decrease) of ΔE_{xp}^l originates from the positive Madelung potential created by the Ca cation, which stabilizes electrons in the vicinity of the Ca cation. When d_{Ca}^z increases, the Ca cation becomes closer to (farther from) the O atoms in the IP (OP). Thus, the $\text{O}2p_\sigma$ orbitals in the IP (OP) are destabilized (stabilized) [see Fig. 14(b)]. The $\text{Cu}3d_{x^2-y^2}$ orbitals are also destabilized, but less than $\text{O}2p_\sigma$ orbitals because Cu atoms are farther from Ca compared to in-plane O. The above simple view is supported by the fact that the variation in $\epsilon_{p_\sigma}^l$ with d_{Ca}^z and the variation in LEH parameters with d_{Ca}^z are twice faster in the IP compared to the OP [see Fig. 14(b) and Fig. 13]. This is because the IP is surrounded by twice as many Ca cations than the OP (see Fig. 2). However, note that the average values of LEH parameters do not vary substantially, because the Δd_{Ca}^z dependencies of LEH parameters in the IP and OP compensate each other. This explains why the increase in $\Delta E_{xp}^{\text{avg}}$ from P_{amb} to P_{opt} originates from P_a rather than P_c (see Sec. V B).

d_{Cu}^z dependence of AB LEH parameters. The optimized value $d_{\text{Cu}}^z \simeq 2.82 \text{ \AA}$ is lower than that from Zhang *et al.* ($d_{\text{Cu}}^z \simeq 2.91 \text{ \AA}$). Thus, we consider $0.0 \text{ \AA} \leq \Delta d_{\text{Cu}}^z \leq +0.2 \text{ \AA}$ to examine the d_{Cu}^z dependence of AB LEH parameters.

Increasing d_{Cu}^z causes the rapid increase in u^i [see Fig. 13(b)], due to the decrease in both v^i and R^i [see Figs. 13(d), 13(e)].

The decrease in v^i is caused by the decrease in ΔE_{xp}^i [see Figs. 13(e), 13(f)]. ΔE_{xp}^i decreases because the in-plane O anions in the OP become farther from those in the IP. As a result, the $\text{O}2p_\sigma$ electrons in the IP are stabilized [see Fig. 14(c)],

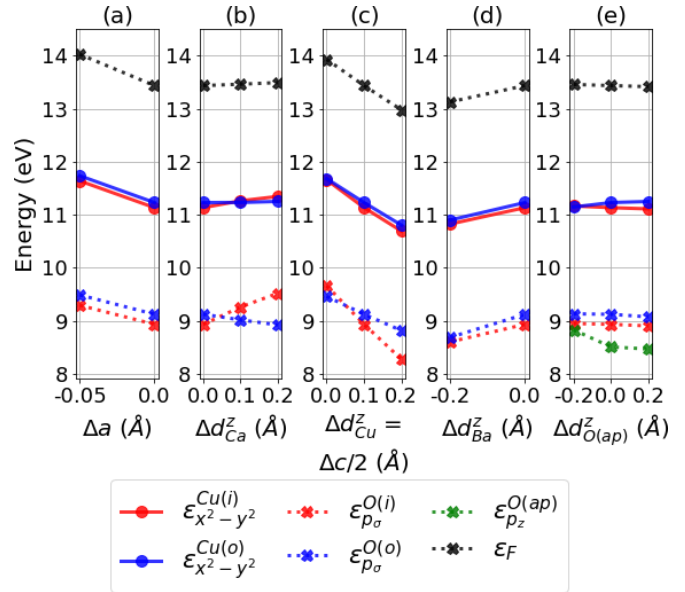


FIG. 14. CP dependencies of the Fermi energy ϵ_F and onsite energies ϵ_i^l of the $\text{Cu}3d_{x^2-y^2}$ and $\text{O}2p_\sigma$ ALWOs. The quantities are obtained using the optimized CP values at $P_{\text{opt}} = 30 \text{ GPa}$, and modifying the values of a , c , and d_i^z by Δa , Δc , and Δd_i^z , respectively. Note that when Δd_{Cu}^z is applied, $\Delta c = 2\Delta d_{\text{Cu}}^z$ is also applied so that all interatomic distances in the block layer remain unchanged. In panel (e), we also show the $d_{\text{O(ap)}}^z$ dependence of the onsite energy $\epsilon_{p_z}^{\text{O(ap)}}$ of the apical $\text{O}2p_z$ orbital.

because the Madelung potential from O anions in the OP is weaker.

However, the decrease in ΔE_{xp}^i may not be sufficient to explain the decrease in R^l . We see that from $\Delta d_{\text{Cu}}^z = 0.0 \text{ \AA}$ to $\Delta d_{\text{Cu}}^z = -0.2 \text{ \AA}$, R^o slightly decreases and R^i sharply decreases [see Fig. 13(d)]. The decrease in R^o is not consistent with the increase in ΔE_{xp}^o which contributes to increase R^o ; also, the decrease in R^i is very sharp compared to the smooth decrease in ΔE_{xp}^i .

Instead, the decrease in R^l may be caused by an increase in cRPA screening between adjacent CuO_2 planes. This is intuitive because $\Delta d_{\text{Cu}}^z = -0.2 \text{ \AA}$ reduces the distance between the CuO_2 planes in the real space. This increases the overlap and hybridization between M-ALWOs in the IP and OP, which may increase the cRPA screening (see also the discussion about the $d_{\text{O(ap)}}^z$ dependence of the screening below). The interplane cRPA screening particularly affects the IP, because the IP is adjacent to two OPs, whereas the OP is adjacent to only the IP; this explains the sharp decrease in R^i .

d_{Ba}^z dependence of AB LEH parameters. The optimized value $d_{\text{Ba}}^z \simeq 1.96 \text{ \AA}$ is similar to that from Zhang *et al.* ($d_{\text{Ba}}^z \simeq 1.98 \text{ \AA}$). Still, for completeness, we consider $-0.2 \text{ \AA} \leq \Delta d_{\text{Ba}}^z \leq 0.0 \text{ \AA}$ in order to examine the d_{Ba}^z dependence of AB LEH parameters.

Decreasing d_{Ba}^z does not cause a significant variation in u^l [see Fig. 13(b)]. Still, we note that v^o and ΔE_{xp}^o slightly increase [see Figs. 13(e) and 13(f)]. This is because the positive Madelung potential from Ba cation felt by the OP is stronger (see the above discussion on the d_{Ca}^z dependence of ΔE_{xp}^l).

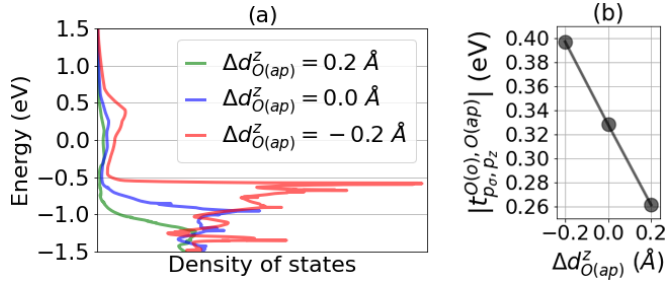


FIG. 15. (a) $\Delta d_{O(\text{ap})}^z$ dependence of the partial density of states of the apical O2p_z M-ALWO. (b) $\Delta d_{O(\text{ap})}^z$ dependence of the amplitude $|t_{p_\sigma, p_z}^{O(o), O(\text{ap})(o)}|$ of the apical O 2p_z/in-plane O2p_σ hopping. The quantities are obtained using the optimized CP values at $P_{\text{opt}} = 30$ GPa, and modifying the value of $d_{O(\text{ap})}^z$ by $\Delta d_{O(\text{ap})}^z$.

Note that the positive Madelung potential from Ba cation does not affect the IP, because the IP is separated from the Ba cation by the OP (see Fig. 2).

$d_{O(\text{ap})}^z$ dependence of AB LEH parameters. The optimized value $d_{O(\text{ap})}^z \simeq 2.22 \text{ \AA}$ is slightly lower than that from Zhang *et al.* ($d_{O(\text{ap})}^z \simeq 2.32 \text{ \AA}$). Thus, we consider $0.0 \text{ \AA} \leq \Delta d_{O(\text{ap})}^z \leq +0.2 \text{ \AA}$ to examine the $d_{O(\text{ap})}^z$ dependence of AB LEH parameters. In addition, we consider $-0.2 \text{ \AA} \leq \Delta d_{O(\text{ap})}^z \leq 0.0 \text{ \AA}$ to probe the effect of apical O displacement at higher pressures.

In the $d_{O(\text{ap})}^z$ dependence of u^o [see Fig. 13(b)], there is a sharp decrease in u^o when $d_{O(\text{ap})}^z$ decreases. This decrease has also been observed in the case of Bi2201 and Bi2212 [30]. It has two origins: (i) the decrease in v^o due to the decrease in ΔE_{xp}^o [see Figs. 13(e) and 13(f)], and more prominently (ii) the decrease in R^o [see Fig. 13(d)]. (ii) is due to the cRPA screening of AB electrons by the apical O, and this screening increases when $d_{O(\text{ap})}^z$ decreases as in Bi2201 and Bi2212 [30]. Note that, contrary to R^o , R^i does not decrease significantly when $d_{O(\text{ap})}^z$ decreases: This is because the IP is protected from the cRPA screening from apical O by the OP, which separates the IP from the apical O (see Fig. 2).

A possible origin of (ii) is the increase in hybridization between the apical O 2p_z orbital and AB orbital in the OP. We show in Fig. 15(a) the partial density of states of the apical O2p_z M-ALWO. We see that bands at the Fermi level have slight apical O2p_z character, in addition to the dominant AB character. This originates from the hybridization between the AB orbital and the apical O2p_z orbital. The apical O2p_z partial density of states at Fermi level increases when $d_{O(\text{ap})}^z$ decreases, which suggests the increase in hybridization between apical O 2p_z and AB orbitals. This is further supported by the increase in amplitude $|t_{p_\sigma, p_z}^{O(o), O(\text{ap})(o)}|$ of the apical O 2p_z/in-plane O2p_σ hopping when $d_{O(\text{ap})}^z$ decreases [see Fig. 15(b)], because the AB orbital is partly constructed from the in-plane O2p_σ orbital.

- [1] J. G. Bednorz and K. A. Müller, Possible high T_c superconductivity in the Ba-La-Cu-O system, *Z. Phys. B* **64**, 189 (1986).
- [2] J. B. Torrance, Y. Tokura, S. J. LaPlaca, T. C. Huang, R. J. Savoy, and A. I. Nazzari, New class of high T_c structures: Intergrowth of multiple copper oxide perovskite-like layers with double sheets of BiO, *Solid State Commun.* **66**, 703 (1988).
- [3] L. Gao, Y. Y. Xue, F. Chen, Q. Xiong, R. L. Meng, D. Ramirez, C. W. Chu, J. H. Eggert, and H. K. Mao, Superconductivity up to 164 K in HgBa₂Ca_{m-1}Cu_mO_{2m+2+δ} ($m = 1, 2,$ and 3) under quasihydrostatic pressures, *Phys. Rev. B* **50**, 4260 (1994).
- [4] P. Dai, B. C. Chakoumakos, G. F. Sun, K. W. Wong, Y. Xin, and D. F. Lu, Synthesis and neutron powder diffraction study of the superconductor HgBa₂Ca₂Cu₃O_{8+δ} by Tl substitution, *Physica C: Supercond.* **243**, 201 (1995).
- [5] A. Yamamoto, N. Takeshita, C. Terakura, and Y. Tokura, High pressure effects revisited for the cuprate superconductor family with highest critical temperature, *Nat. Commun.* **6**, 8990 (2015).
- [6] M. Nuñez-Regueiro, J. L. Tholence, E. V. Antipov, J. J. Capponi, and M. Marezio, Pressure-induced enhancement of T_c above 150 K in Hg-1223, *Science* **262**, 97 (1993).
- [7] M. T. Schmid, J.-B. Morée, R. Kaneko, Y. Yamaji, and M. Imada, Superconductivity studied by solving *ab initio* low-energy effective Hamiltonians for carrier doped CaCuO₂, Bi₂Sr₂CuO₆, Bi₂Sr₂CaCu₂O₈, and HgBa₂CuO₄, *Phys. Rev. X* **13**, 041036 (2023).
- [8] M. F. Crommie, A. Y. Liu, A. Zettl, M. L. Cohen, P. Parilla, M. F. Hundley, W. N. Creager, S. Hoen, and M. S. Sherwin, *c*-axis stress dependence of normal and superconducting state properties of YBa₂Cu₃O₇, *Phys. Rev. B* **39**, 4231 (1989).
- [9] C. Meingast, O. Kraut, T. Wolf, H. Wühl, A. Erb, and G. Müller-Vogt, Large *a-b* anisotropy of the expansivity anomaly at T_c in untwinned YBa₂Cu₃O_{7-δ}, *Phys. Rev. Lett.* **67**, 1634 (1991).
- [10] G. L. Belenky, S. M. Green, A. Roytburd, C. J. Lobb, S. J. Hagen, R. L. Greene, M. G. Forrester, and J. Talvacchio, Effect of stress along the *ab* plane on the J_c and T_c of YBa₂Cu₃O₇ thin films, *Phys. Rev. B* **44**, 10117 (1991).
- [11] U. Welp, M. Grimsditch, S. Fleshler, W. Nessler, J. Downey, G. W. Crabtree, and J. Guimpel, Effect of uniaxial stress on the superconducting transition in YBa₂Cu₃O₇, *Phys. Rev. Lett.* **69**, 2130 (1992).
- [12] C. Meingast, J. Karpinski, E. Jilek, and E. Kaldis, Uniaxial pressure dependence of T_c of single crystalline YBa₂Cu₄O₈ via thermal expansion, *Physica C: Supercond.* **209**, 591 (1993).
- [13] M. Mito, T. Imakyurei, H. Deguchi, K. Matsumoto, T. Tajiri, H. Hara, T. Ozaki, H. Takeya, and Y. Takano, Uniaxial strain effects on cuprate superconductor YBa₂Cu₄O₈, *J. Phys. Soc. Jpn.* **81**, 113709 (2012).
- [14] M. Mito, H. Matsui, T. Imakyurei, H. Deguchi, T. Horide, K. Matsumoto, A. Ichinose, and Y. Yoshida, Effects of selective lattice deformation on YbBa₂Cu₄O₈ and YBa₂Cu₃O₇ epitaxial films, *Appl. Phys. Lett.* **104**, 102601 (2014).
- [15] M. Mito, T. Imakyurei, H. Deguchi, K. Matsumoto, H. Hara, T. Ozaki, H. Takeya, and Y. Takano, Effective disappearance of the Meissner signal in the cuprate superconductor YBa₂Cu₄O₈ under uniaxial strain, *J. Phys. Soc. Jpn.* **83**, 023705 (2014).
- [16] M. Mito, H. Goto, H. Matsui, H. Deguchi, K. Matsumoto, H. Hara, T. Ozaki, H. Takeya, and Y. Takano, Uniaxial strain

effects on superconducting transition in $Y_{0.98}Ca_{0.02}Ba_2Cu_4O_8$, *J. Phys. Soc. Jpn.* **85**, 024711 (2016).

[17] F. Hardy, N. J. Hillier, C. Meingast, D. Colson, Y. Li, N. Barišić, G. Yu, X. Zhao, M. Greven, and J. S. Schilling, Enhancement of the critical temperature of $HgBa_2CuO_{4+\delta}$ by applying uniaxial and hydrostatic pressure: Implications for a universal trend in cuprate superconductors, *Phys. Rev. Lett.* **105**, 167002 (2010).

[18] M. Mito, K. Ogata, H. Goto, K. Tsuruta, K. Nakamura, H. Deguchi, T. Horide, K. Matsumoto, T. Tajiri, H. Hara *et al.*, Uniaxial strain effects on the superconducting transition in Re-doped Hg-1223 cuprate superconductors, *Phys. Rev. B* **95**, 064503 (2017).

[19] S. N. Putilin, E. V. Antipov, O. Chmaissem, and M. Marezio, Superconductivity at 94 K in $HgBa_2CuO_{4+\delta}$, *Nature (London)* **362**, 226 (1993).

[20] P. Hohenberg and W. Kohn, Inhomogeneous electron gas, *Phys. Rev.* **136**, B864 (1964).

[21] W. Kohn and L. J. Sham, Self-consistent equations including exchange and correlation effects, *Phys. Rev.* **140**, A1133 (1965).

[22] F. Aryasetiawan, M. Imada, A. Georges, G. Kotliar, S. Biermann, and A. I. Lichtenstein, Frequency-dependent local interactions and low-energy effective models from electronic structure calculations, *Phys. Rev. B* **70**, 195104 (2004).

[23] F. Aryasetiawan, K. Karlsson, O. Jepsen, and U. Schönberger, Calculations of Hubbard U from first principles, *Phys. Rev. B* **74**, 125106 (2006).

[24] M. Imada and T. Miyake, Electronic structure calculation by first principles for strongly correlated electron systems, *J. Phys. Soc. Jpn.* **79**, 112001 (2010).

[25] M. Hirayama, T. Miyake, and M. Imada, Derivation of static low-energy effective models by an *ab initio* downfolding method without double counting of Coulomb correlations: Application to $SrVO_3$, $FeSe$, and $FeTe$, *Phys. Rev. B* **87**, 195144 (2013).

[26] M. Hirayama, T. Misawa, T. Miyake, and M. Imada, *Ab initio* studies of magnetism in the iron chalcogenides $FeTe$ and $FeSe$, *J. Phys. Soc. Jpn.* **84**, 093703 (2015).

[27] M. Hirayama, Y. Yamaji, T. Misawa, and M. Imada, *Ab initio* effective Hamiltonians for cuprate superconductors, *Phys. Rev. B* **98**, 134501 (2018).

[28] M. Hirayama, T. Misawa, T. Ohgoe, Y. Yamaji, and M. Imada, Effective Hamiltonian for cuprate superconductors derived from multiscale *ab initio* scheme with level renormalization, *Phys. Rev. B* **99**, 245155 (2019).

[29] T. Ohgoe, M. Hirayama, T. Misawa, K. Ido, Y. Yamaji, and M. Imada, *Ab initio* study of superconductivity and inhomogeneity in a Hg-based cuprate superconductor, *Phys. Rev. B* **101**, 045124 (2020).

[30] J.-B. Morée, M. Hirayama, M. T. Schmid, Y. Yamaji, and M. Imada, *Ab initio* low-energy effective Hamiltonians for the high-temperature superconducting cuprates $Bi_2Sr_2CuO_6$, $Bi_2Sr_2CaCu_2O_8$, $HgBa_2CuO_4$, and $CaCuO_2$, *Phys. Rev. B* **106**, 235150 (2022).

[31] M. Hirayama, M. T. Schmid, T. Tadano, T. Misawa, and M. Imada, *Ab initio* material design of Ag-based oxides for high- T_c superconductor, [arXiv:2207.12595](https://arxiv.org/abs/2207.12595).

[32] See Supplemental Material at <http://link.aps.org/supplemental/10.1103/PhysRevResearch.6.023163> for the complete list of parameters for the effective Hamiltonians presented in the main text.

[33] X. Zhang, W. H. Lu, and C. K. Ong, Structural changes in $HgBa_2Ca_2Cu_3O_{8+\delta}$ under high pressure, *Physica C: Supercond.* **289**, 99 (1997).

[34] A. R. Armstrong, W. I. F. David, I. Gameson, P. P. Edwards, J. J. Capponi, P. Bordet, and M. Marezio, Crystal structure of $HgBa_2Ca_2Cu_3O_{8+\delta}$ at high pressure (to 8.5 GPa) determined by powder neutron diffraction, *Phys. Rev. B* **52**, 15551 (1995).

[35] B. A. Hunter, J. D. Jorgensen, J. L. Wagner, P. G. Radaelli, D. G. Hinks, H. Shaked, R. L. Hitterman, and R. B. Von Dreele, Pressure-induced structural changes in superconducting $HgBa_2Ca_{n-1}Cu_nO_{2n+2+\delta}$ ($n = 1, 2, 3$) compounds, *Physica C: Supercond.* **221**, 1 (1994).

[36] J. H. Eggert, J. Z. Hu, H. K. Mao, L. Beauvais, R. L. Meng, and C. W. Chu, Compressibility of the $HgBa_2Ca_{n-1}Cu_nO_{2n+2+\delta}$ ($n = 1, 2, 3$) high-temperature superconductors, *Phys. Rev. B* **49**, 15299 (1994).

[37] P. Bordet, S. Le Floch, J. J. Capponi, C. Chaillout, M. F. Gorius, M. Marezio, J. L. Tholence, and P. G. Radaelli, Gold substitution in mercury cuprate superconductors, *Physica C: Supercond.* **262**, 151 (1996).

[38] H. Kotegawa, Y. Tokunaga, K. Ishida, G.-Q. Zheng, Y. Kitaoka, H. Kito, A. Iyo, K. Tokiwa, T. Watanabe, and H. Ihara, Unusual magnetic and superconducting characteristics in multilayered high- T_c cuprates: ^{63}Cu NMR study, *Phys. Rev. B* **64**, 064515 (2001).

[39] K. Nakamura, Y. Yoshimoto, Y. Nomura, T. Tadano, M. Kawamura, T. Kosugi, K. Yoshimi, T. Misawa, and Y. Motoyama, RESPACK: An *ab initio* tool for derivation of effective low-energy model of material, *Comput. Phys. Commun.* **261**, 107781 (2021).

[40] H. Sakakibara, K. Suzuki, H. Usui, K. Kuroki, R. Arita, D. J. Scalapino, and H. Aoki, Multiorbital analysis of the effects of uniaxial and hydrostatic pressure on T_c in the single-layered cuprate superconductors, *Phys. Rev. B* **86**, 134520 (2012).

[41] K. Momma and F. Izumi, VESTA3 for three-dimensional visualization of crystal, volumetric and morphology data, *J. Appl. Crystallogr.* **44**, 1272 (2011).

[42] T. Misawa, S. Morita, K. Yoshimi, M. Kawamura, Y. Motoyama, K. Ido, T. Ohgoe, M. Imada, and T. Kato, mVMC—open-source software for many-variable variational Monte Carlo method, *Comput. Phys. Commun.* **235**, 447 (2019).

[43] D. Wu, R. Rossi, F. Vicentini, N. Astrakhantsev, F. Becca, X. Cao, J. Carrasquilla, F. Ferrari, A. Georges, M. Hibat-Allah *et al.*, Variational benchmarks for quantum many-body problems, [arXiv:2302.04919](https://arxiv.org/abs/2302.04919).

[44] K. Held, C. Taranto, G. Rohringer, and A. Toschi, Hedin equations, GW, GW+DMFT, and all that, [arXiv:1109.3972](https://arxiv.org/abs/1109.3972).

[45] F. Krien, A. Kauch, and K. Held, Tiling with triangles: Parquet and $GW\gamma$ methods unified, *Phys. Rev. Res.* **3**, 013149 (2021).

[46] B. Cunningham, M. Grüning, D. Pashov, and M. van Schilfgaarde, QS \widehat{GW} : Quasiparticle self-consistent GW with ladder diagrams in W , *Phys. Rev. B* **108**, 165104 (2023).

[47] S. Acharya, C. Weber, E. Plekhanov, D. Pashov, A. Taraphder, and M. Van Schilfgaarde, Metal-insulator transition in copper oxides induced by apex displacements, *Phys. Rev. X* **8**, 021038 (2018).

- [48] S. Acharya, M. I. Katsnelson, and M. van Schilfgaarde, Vertex dominated superconductivity in intercalated FeSe, *npj Quantum Mater.* **8**, 24 (2023).
- [49] P. Giannozzi, S. Baroni, N. Bonini, M. Calandra, R. Car, C. Cavazzoni, D. Ceresoli, G. L. Chiarotti, M. Cococcioni, I. Dabo *et al.*, QUANTUM ESPRESSO: A modular and open-source software project for quantum simulations of materials, *J. Phys.: Condens. Matter* **21**, 395502 (2009).
- [50] P. Giannozzi Jr, O. Andreussi, T. Brumme, O. Bunau, M. B. Nardelli, M. Calandra, R. Car, C. Cavazzoni, D. Ceresoli, M. Cococcioni *et al.*, Advanced capabilities for materials modelling with QUANTUM ESPRESSO, *J. Phys.: Condens. Matter* **29**, 465901 (2017).
- [51] M. Schlipf and F. Gygi, Optimization algorithm for the generation of ONCV pseudopotentials, *Comput. Phys. Commun.* **196**, 36 (2015).
- [52] J. P. Perdew, K. Burke, and M. Ernzerhof, Generalized gradient approximation made simple, *Phys. Rev. Lett.* **77**, 3865 (1996).
- [53] <http://www.quantum-espresso.org>
- [54] L. Nordheim, The electron theory of metals, *Ann. Phys.* **401**, 607 (1931).
- [55] N. Marzari and D. Vanderbilt, Maximally localized generalized Wannier functions for composite energy bands, *Phys. Rev. B* **56**, 12847 (1997).
- [56] I. Souza, N. Marzari, and D. Vanderbilt, Maximally localized Wannier functions for entangled energy bands, *Phys. Rev. B* **65**, 035109 (2001).
- [57] T. Miyake, F. Aryasetiawan, and M. Imada, *Ab initio* procedure for constructing effective models of correlated materials with entangled band structure, *Phys. Rev. B* **80**, 155134 (2009).
- [58] T. Misawa and M. Imada, Quantum criticality around metal-insulator transitions of strongly correlated electron systems, *Phys. Rev. B* **75**, 115121 (2007).